LUND UNIVERSITY

Interacting fermions in 1D disordered lattices: Exploring localization and transport properties with lattice density-functional theories

Vettchinkina, Valeria; Kartsev, Alexey; Karlsson, Daniel; Verdozzi, Claudio

Link to publication

Interacting fermions in one-dimensional disordered lattices: Exploring localization and transport properties with lattice density-functional theories

V. Vettchinkina, A. Kartsev, D. Karlsson, and C. Verdozzi

Mathematical Physics and European Theoretical Spectroscopy Facility (ETSF), Lund University, 22100 Lund, Sweden

We investigate the static and dynamical behavior of one-dimensional interacting fermions in disordered Hubbard chains contacted to semi-infinite leads. The chains are described via the repulsive Anderson-Hubbard Hamiltonian, using static and time-dependent lattice density-functional theory. The dynamical behavior of our quantum transport system is studied using an integration scheme available in the literature, which we modify via the recursive Lanczos method to increase its efficiency. To quantify the degree of localization due to disorder and interactions, we adapt the definition of the inverse participation ratio to obtain an indicator which is suitable for quantum transport geometries and can be obtained within density-functional theory. Lattice density-functional theories are reviewed and, for contacted chains, we analyze the merits and limits of the coherent-potential approximation in describing the spectral properties, with interactions included via lattice density-functional theory. Our approach appears to be able to capture complex features due to the competition between disorder and interactions. Specifically, we find a dynamical enhancement of delocalization in the presence of a finite bias and an increase of the steady-state current induced by interparticle interactions. This behavior is corroborated by results for the time-dependent densities and for the inverse participation ratio. Using short isolated chains with interaction and disorder, a brief comparative analysis between time-dependent density-functional theory and exact results is then given, followed by general concluding remarks.

I. INTRODUCTION

In many physical phenomena, practical limitations hinder a complete knowledge of all the degrees of freedom involved. Nanoscience has adopted such apparent shortcoming as its central paradigm, by exploiting the notion of a small system coupled to a macroscopic environment. A case in point is represented by nanoscale transport phenomena, where two (or more) macroscopic leads are connected to small central devices (quantum constriction).[1,2]

Such devices, whose sizes range from that of few atoms (as in short nanowires or small molecules) to that of several repeated large molecular units, attract scientific interest because they are seen as possible candidates for novel electronic, spintronic, or quantum computation devices, to mention a few.[3] This, in turn, requires a thorough understanding and control of the decoherence processes which can affect carrier propagation and manipulation in the device region.

In this work we consider two of such processes, namely disorder and interparticle interactions (thus leaving out other important decoherence mechanisms, e.g., lattice vibrations). How interactions and disorder affect the conduction properties of materials has been intensively investigated over several decades,[4–16] and significant progress has been made. However, some issues remain to a considerable extent open, e.g., the real-time dynamics of samples with disorder and interactions.

Starting with the seminal paper by Anderson,[4] lattice models have had an eminent place in the study of disordered systems with and without interactions. While a large fraction of the literature on disordered interacting lattice models concentrates on the equilibrium regime (for both finite and extended systems), more recently the time-dependent properties have also been examined, primarily for finite samples.[17,18] In between the finite/infinite-system categories, a third one is

represented by small disordered samples connected to semi-infinite homogenous reservoirs,[19] of relevance to quantum transport phenomena.

This paper looks into some aspects of the transport properties of 1D interacting fermions in disordered lattice systems, using static[20] and time-dependent density-functional theory[21] (DFT and TDDFT, respectively) in the lattice version. Static and time-dependent DFT are, in principle, exact reformulations of the (time-dependent) many-body problem,[22] where the key variable is the one-particle density n, and a central ingredient is the exchange-correlation (XC) potential v_{xc} (recent comprehensive reviews of the subject are Refs. 23–25). The XC potential embodies the complexities of the many-body problem. In this contracted description, v_{xc} is a highly nontrivial functional of the density (in TDDFT, where time enters explicitly into the formulation, such functional dependence includes the entire history of the density n, i.e., memory effects). In general, the exact v_{xc} is not known, and approximations are introduced. A simple but not always adequate prescription is the so-called (adiabatic) local density approximation, where the XC potential depends only on the local (time-dependent) density. This amounts to neglecting nonlocality in space (and memory effects in the TD case) in v_{xc}. As a result of this oversimplification, in some practical applications an accurate description of dynamical interparticle correlations may be lacking.

The application of static density-functional theories to lattice models started almost 30 years ago,[26–29] and in the last decade this approach has been further developed.[30–39] On the other hand, the use of lattice TDDFT to describe the nonequilibrium dynamics of Hubbard-like models is a rather new topic[40–43]; firm conceptual ground was initially established for approaches based on lattice bond currents,[44–46]

while a rigorous formulation using the density as the basic variable[47] has been provided only very recently.

After the above, somewhat lengthy, considerations, we can now define the motivations behind this work and the chosen methodology. Our focus is on finite chains contacted to semi-infinite leads, with short-range interactions and disorder present only in the chains (the "device"). Even within these narrow boundaries, the issues which can potentially be addressed are many, but we only touch upon a few of them and go into no great detail. In this respect, our work is somewhat exploratory in character, since we also describe some methodological developments that we found necessary when using (TD)DFT for disordered lattice systems in the quantum transport regime. Concerning the chosen methodology, we note that, compared to other lattice approaches, lattice (TD)DFT is well suited for any dimensionality and is relatively inexpensive from the computational point of view (since it deals with single-particle orbitals). These are attractive features when, for example, one needs to perform configuration averages of time-evolved quantities in the long-time limit (such as when approaching the steady-state regime in a quantum transport setup with disordered samples).

The outline of the paper is as follows. In Sec. II, we describe the lattice model system that we employ in our work. In Sec. III, we present the lattice (TD)DFT formalism and describe how to obtain the XC potential from the exact solution of the one-dimensional (1D) Hubbard model. This is accompanied by a review of the inherent literature to illustrate the developments and applications that have occurred so far within this approach. In Sec. IV, which deals with disorder, we first discuss the inverse participation ratio; then we introduce a formulation for contacted chains based on the coherent-potential approximation and DFT. In Sec. V we start by briefly reviewing lattice TDDFT approaches to quantum transport. Then we present in some detail a method recently proposed in the literature,[48] followed by a description of our modifications to it, to increase its efficiency. Some technical details relative to Secs. IV and V are relegated to Appendices A and B. In Sec. VI, we report and discuss our results for static and nonequilibrium regimes. Our conclusions are in Sec. VII.

II. THE MODEL

In standard notation, the lattice systems considered in this paper are described by the following Hamiltonian:

$$
\begin{aligned}
H = & -\sum_{\sigma}\sum_{l=-\infty}^{\infty} V_{l,l+1}(a_{l\sigma}^{\dagger}a_{l+1,\sigma} + \text{H.c.}) \\
& + \sum_{\sigma}\sum_{l=1}^{L}\left[w_l(\tau) + \frac{U}{2}\hat{n}_{l-\sigma}\right]\hat{n}_{l\sigma} + b_S(\tau)\sum_{l<1;\sigma}\hat{n}_{l\sigma} \\
& + b_D(\tau)\sum_{l>L;\sigma}\hat{n}_{l\sigma}.
\end{aligned}
\tag{1}
$$

Equation (1) describes a central chain of length L (the lattice sites with $1 \leqslant l \leqslant L$) connected to a left and a right 1D lead (sites with $l < 1$ and $l > L$, respectively). The third and fourth terms in Eq. (1) represent the time-dependent bias in the leads (τ is the time variable), which is applied at time $\tau \geqslant 0$ [often, in

the literature, the leads are also referred to as the source (S) and drain (D), hence the subscripts S, D in the bias terms in Eq. (1)]. For the contacted chain, the hopping term $V_{l,l+1} = V$ always; i.e., we employ transparent boundary conditions (hereafter, $V \equiv 1$ is taken as the energy unit). The Hamiltonian of the isolated chain is obtained from the general one by putting $V_{0,1} = V_{L,L+1} = 0$ in Eq. (1) and retaining only the sites labeled by $1 \leqslant l \leqslant L$. Looking more closely to the chain part of the Hamiltonian, we have Hubbard-like interactions (the term proportional to U; we set $U > 0$) and time-dependent on-site energies $w_l(\tau)$, which is convenient to separate into static and time-dependent parts: $w_l(\tau) = \epsilon_l + v_l(\tau)$. In the presence of disorder, the ϵ_l's are distributed according to some disorder probability distribution. In this work, we use primarily the box disorder distribution, i.e., $\epsilon_l \in [-W/2, W/2]$, but, we sometimes consider binary disorder, where $\epsilon_l = \pm W$. In both cases, W fixes the strength of the disorder. The chain Hamiltonian is a finite-size realization of the so-called Anderson-Hubbard model (AHM),[10] one of the most used models to study strongly correlated and disordered systems.[16] The AHM generalizes the standard Hubbard Hamiltonian[49] to inhomogeneous (and, in our case, possibly time-dependent) situations. That is, $\hat{\mathcal{V}}(\tau) \equiv \sum_{l\sigma} v_l(\tau)\hat{n}_{l\sigma}$ describes a local (in space and time), time-dependent potential in the chain. In the static case (i.e., before the systems start to time evolve), all $v_l(\tau) = 0$. Furthermore, the usual Hubbard model for the chain[49] is recovered when $w_l(\tau) = 0$, while, when $U = 0$ but $\epsilon_l \neq 0$, the chain is described the so-called Anderson model of disorder.[4]

III. (TD)DFT FOR LATTICE MODELS

A. General aspects of lattice (TD)DFT

A DFT based on the site occupation numbers n_R was introduced more than two decades ago to describe some ground-state properties of the Hubbard model.[26–28] An exact LDA (based on the Bethe ansatz) for the inhomogeneous 1D Hubbard model was first considered in Ref. 29. Further significant progress came when an explicit and simple expression for the XC functional based on the Bethe ansatz was provided[30] and practically used to investigate different inhomogeneous Hubbard-type models. In subsequent work, The LDA based on the Bethe ansatz for v_{xc} was scrutinized against exact results,[30–32,50,51] providing energies, particle densities, and entropies with an accuracy within a few percent (for alternative DFT-like formulations on the lattice problem, see, e.g., Refs. 52–54).

Recently, lattice DFT has also been used to determine the polarizability of the 1D Hubbard model,[55] the effect of surfaces,[56] and also to study the entanglement entropy of the Hubbard model.[51] Furthermore, explicit analytical expressions for the XC potentials in small clusters can be found in Ref. 57, while the role of the temperature on v_{xc} has been discussed in Refs. 38,39,58. Lattice (TD)DFT has also been used to investigate ultracold atoms loaded on optical lattices.[32,39,43,59–62] These systems make it possible to study different ground-state and nonequilibrium scenarios for the Hubbard model[63] with high accuracy (because a precise tunability of the lattice parameters is possible) more

directly and easily than in solid-state experiments. In 2D, the Hubbard model has been investigated via DFT on the graphene lattice.[64] To date, the simple cubic lattice is the only 3D case considered in the literature,[62] with the ground-state energy of the uniform system computed within dynamical mean field theory (DMFT).[65,66] Differently from the 1D case, here a discontinuity in v_{xc} appears only for $U > U_c^{\text{Mott}}$, a DFT description of the onset of the Mott-Hubbard metal-insulator regime at a finite U.

Very recently, lattice TDDFT has been rigorously formulated as a Cauchy problem for a nonlinear Schrödinger equation,[47] and both uniqueness and v_0-representability theorems have been demonstrated (for early discussions of v_0 representability on the lattice, see Refs. 40–42). In this respect, it may be worth noting that a direct adaptation of the Runge-Gross formulation[21] to the lattice case is not possible[44] (historically, rigorous formulations on the lattice used at first the bond-current, instead of the density, as the basic variable[44–46]). Lattice (TD)DFT has also been considered for quantum transport geometries: This aspect is examined in Sec. V below.

B. Formulation

In this paper, we confine ourselves to the 1D case; we review here the actual formulation for spin-independent (TD)DFT. In standard DFT notation, we can write for the ground-state total energy[28,29]:

$$E[n, v_{\text{ext}}] \equiv T_0[n] + E_H[n] + E_{xc}[n] + \sum_i v_{\text{ext}}(i) n_i, \quad (2)$$

where $v_{\text{ext}}(i) \equiv \epsilon_i$ is the static external field, and $T_0[n]$ and $E_H = \frac{1}{4} \sum_i U_i n_i^2$ are, respectively, the noninteracting kinetic energy and the Hartree energy, with $n_i = \sum_\sigma n_{i\sigma}$. To perform a local density approximation, E_{xc} is obtained from a homogeneous reference system (Hubbard model):

$$E_{xc} = E - T_0 - E_H. \quad (3)$$

To obtain v_{xc}, one takes the derivative of the XC energy per site $e_{xc} \equiv E_{xc}/L$ with respect to the density (in the general case, this should be a functional derivative):

$$v_{xc} = \frac{\partial e_{xc}(n, U)}{\partial n}. \quad (4)$$

For bipartite lattices, $e_{xc}(n, U) = e_{xc}(2 - n, U)$ in the entire density range $[0,2]$ and thus $v_{xc}(n) = -v_{xc}(2 - n)$. Finally, a local density approximation is defined:

$$v_{xc}(i) = v_{xc}(n_i). \quad (5)$$

In ground-state DFT-LDA calculations, the XC potential obtained in this way is used to solve self-consistently the Kohn-Sham (KS) equations

$$(\hat{t} + \hat{v}_{KS})\varphi_\kappa = \varepsilon_\kappa \varphi_\kappa, \quad (6)$$

where $\hat{t}$ denotes the matrix for the single-particle hoppings between nearest-neighboring sites and φ_κ is the κth single-particle KS orbital, with $n_i = \sum_{\kappa \in occ} |\varphi_\kappa(i)|^2$. The effective potential matrix is diagonal: $(\hat{v}_{KS})_{ii} = v_{KS}(i) = v_H(i) + v_{xc}(i) + v_{\text{ext}}(i)$, with $v_H(i) = \frac{1}{2} U_i n_i$ being the Hartree potential.

If DFT can be a viable route to describe the ground-state properties of Hubbard-type models, then the lattice KS equations could be propagated in time, to get a TDDFT description of the dynamics of lattice systems. For 1D Hubbard-type Hamiltonians, work in this direction was performed in Refs. 67–69 for the linear response regime. A TDDFT approach to the real-time dynamics of the Hubbard model out of equilibrium was first considered in Ref. 41, where exact results for the density and the XC potentials were compared to those obtained by solving the time-dependent KS equations,

$$(\hat{t} + \hat{v}_{KS}(\tau))\varphi_\kappa(\tau) = i\partial_\tau \varphi_\kappa(\tau). \quad (7)$$

In general, $v_{KS}(i, \tau) = v_H(i, \tau) + v_{xc}(i, \tau) + v_{\text{ext}}(i, \tau)$ depends nonlocally on the density via v_{xc}. The adiabatic local density approximation (ALDA)[70] to the XC potential is then obtained with the prescription $v_{xc}^{ALDA}(i, \tau) \equiv v_{xc}^{LDA}(n_i(\tau))$, where the TD density is given by $n_i(\tau) = \sum_\kappa^{occ} |\varphi_\kappa(i, \tau)|^2$. An ALDA for the Hubbard model was first introduced in Ref. 41, with the treatment limited to spin-compensated systems, while the spin-dependent case was presented in Ref. 43, where TDDFT results and time-dependent DMRG (tDMRG) results were compared.

For finite systems, a study more focused on the role of non-local and memory effects beyond the ALDA was performed in Ref. 71, via the ALDA, exact, and Kadanoff-Baym time evolution in small cubic Hubbard clusters. The Kadanoff-Baym equations (KBEs), with a many-body perturbation-theory approach to the self-energy, make it possible to take into account nonlocality and memory effects on equal footing. Such comparisons showed that an ALDA coming from the appropriate (strongly correlated) reference system can perform well in many instances, (especially for slow perturbations) but, quite generally, it will fail for fast perturbations or very strong interactions.

We conclude this section with a remark about notation: The one adopted throughout the paper is fully consistent with the continuum case, i.e., as if the Hubbard interaction was treated as spin-independent: $\hat{U} = \frac{1}{2} \sum_i U_i(\hat{n}_i^2 - \hat{n}_i)$. However, when the interaction is rewritten as in Eq. (1) the interaction is effectively kept among opposite spins (i.e., treated as spin-dependent)[72] and the exchange has been removed at the Hamiltonian level. Thus, e_{xc} and v_{xc} in Eqs. (3) and (4) contain only correlation, and the Hartree plus exchange potential is $U n_i/2$. More aptly, our DFT quantities could have been called e_c and v_c but, following a common practice in the literature on lattice (TD)DFT, we still denote them by e_{xc} and v_{xc}.

C. Obtaining v_{xc} for the 1D Hubbard model

According to Eq. (3), to construct a LDA in 1D we need the exact ground-state energy of the infinite homogeneous 1D Hubbard model, where the hopping $V_{l,l+1} \equiv V$ and the interaction is present at all sites. This requires[29,30,32,55] to solve the coupled Bethe ansatz equations for the charge and spin distribution functions [$\rho(x)$ and $\sigma(x)$, respectively].[73] An ALDA is then easily obtained,[41,43] making v_{xc} become a function of the instantaneous local density. In the nonmagnetic case considered here (where the spin-up and spin-down densities are equal, i.e., $n_\uparrow = n_\downarrow = n/2$), the Bethe ansatz

equations read (x, y denote wave-vector variables)

$$\rho(x) = \frac{1}{2\pi} + \frac{\cos x}{\pi} \int_{-\infty}^{+\infty} \frac{u/4}{(u/4)^2 + (y - \sin x)^2} \sigma(y) dy, \tag{8}$$

$$\sigma(y) = \frac{1}{\pi} \int_{-Q}^{+Q} \frac{u/4}{(u/4)^2 + (y - \sin x)^2} \rho(x) dx$$
$$- \frac{1}{\pi} \int_{-\infty}^{+\infty} \frac{u/2}{(u/2)^2 + (y - y')^2} \sigma(y') dy', \tag{9}$$

with $u \equiv U/V$. The functions $\rho(x)$ and $\sigma(x)$ are related to the charge $n = n_\uparrow + n_\downarrow$ and spin-down $n_\downarrow$ densities via

$$\int_{-Q}^{+Q} \rho(x) dx = n, \quad \int_{-\infty}^{+\infty} \sigma(y) dy = n_\downarrow, \tag{10}$$

from which the integration limit Q is determined. The ground-state energy density for $n_\downarrow = n_\uparrow$ is given by

$$e(n_\uparrow = n_\downarrow, U) = -2V \int_{-Q}^{+Q} \rho(x) \cos x \, dx. \tag{11}$$

Equations (8)–(11) are the prescription used in this work to determine e_{xc}. The numerical solution of Eqs. (8) and (9) was obtained via a self-consistent procedure, with Q adjusted at each iteration via the normalization condition in Eq. (10). Numerical integrations were performed with a 128-point Gauss-Legendre quadrature and, for each U, $e_{xc}(n, U)$ was obtained at the nodes of a uniform mesh for the density n. To obtain v_{xc} at each node of the density mesh, we computed $\delta e_{xc}/\delta n$ with a 5-point numerical derivative. To calculate v_{xc} at off-node densities, a linear interpolation between the the closest nodes was employed. The v_{xc} thus obtained is discontinuous at half filling, as it should be for the homogeneous 1D Hubbard model; however, for a finite interacting system contacted to noninteracting leads, the discontinuity of the exact v_{xc} becomes slightly smoothed (this was indicated in Ref. 74, using support from small Anderson clusters, and fully discussed in Refs. 58,75–77). According to these considerations, and also for numerical convenience, the XC potential was slightly smoothed in our actual calculations.

IV. THE ROLE OF DISORDER

Methodologically, the way we numerically deal with disorder effects in this paper is straightforward, since in most cases we limit our analysis to the arithmetic (configuration) average of specific quantities: the inverse participation ratio (IPR), the density, and the current density. In most cases, the numerical configuration averages are performed over an incomplete set of configurations. Sections IV A and IV B constitute an exception. In these sections, which deal with ground-state quantities, and for the case of binary disorder, we also perform complete numerical averaging over all the configurations to provide benchmark results. For brevity, in the following, complete numerical averaging is referred to as "exact averaging."

A. The inverse participation ratio

A quantity often used as an indicator of localization in a system is the so-called IPR ζ. The original definition[78] of ζ, in-

troduced for noninteracting disordered systems, characterizes a given one-particle quantum state ψ as follows:

$$\zeta_0 = \sum_i^M n_i^2 \bigg/ \left(\sum_i^M n_i \right)^2, \tag{12}$$

where $n_i = |\psi_i|^2$ is the density at site i and the sums extend to all the sites M in the system. For completely localized states (when $\psi \neq 0$ at only one site) we get $\zeta_0 = 1$, while ζ_0 is smallest for delocalized states. To deal with interacting systems, suitable modifications of Eq. (12) are, for example,

$$\zeta_1 = \sum_i^M \Delta n_i^2 \bigg/ \left(\sum_i^M \Delta n_i \right)^2, \tag{13}$$

$$\zeta_2(\omega) = \sum_i^M n_i^2(\omega) \bigg/ \left[\sum_i^M n_i(\omega) \right]^2. \tag{14}$$

The use of ζ_1 is convenient when dealing with small systems with discrete many-body levels.[79] In this case, for N particles, Δn_i is the difference between the ground-state densities with $N + 1$ and N particles, a clear operational prescription for finite systems. Using ζ_2 (Ref. 80) amounts to considering the density of states as obtained from the one-particle propagator, since $n_i(\omega) = -\text{Im} G_{ii}(\omega)/\pi$. It should be noted that most investigations of the IPR are done numerically, for finite systems. Using ζ_2 requires introducing a finite artificial broadening γ, and employing a finite-size scaling analysis, to assess the role of γ.[81–83]

In this work, we study finite disordered systems (short chains) contacted to semi-infinite homogenous leads. While the definition of IPR via Eq. (14) is, in principle, suitable, for our lead-device-lead system we are faced with two issues. (i) A sum is implied over all the sites M in the system, including the leads; this considerably increases the difficulty of the calculation. (ii) More fundamentally, the IPR defined in this way can reflect the properties of the leads rather than the actual systems, since the lead contribution can dominate the sums in Eq. (14). In view of this, we suggest the following possible alternative definition of the energy-dependent IPR:

$$\zeta_3 = \sum_{i \in C} n_i^2(\omega) \bigg/ \left[\sum_{i \in C} n_i(\omega) \right]^2; \tag{15}$$

i.e., the sum is confined to the region of the device. This modified definition of the IPR is further analyzed and compared to the standard one in Sec. VI A.

B. The coherent potential approximation

Among the possible theoretical approaches to disorder, an important place is occupied by the coherent-potential approximation[84–86] (CPA), which introduces a simplified, approximate treatment of disorder averaging.[85–88] A major appeal of CPA in its simplest formulation is the pedagogical value, a relative analytical simplicity and ease of numerical implementation, together with the ability to give results for several quantities (e.g., ground-state energies, transport properties, phase stability, photoemission), which are generally in broad agreement with experiment. Furthermore, the CPA becomes exact in the $D = \infty$ limit[89]; in finite dimensions,

it has been numerically tested against accurate numerical averaging[90] and it has also been used in conjunction with many-body perturbation theory (see, e.g. Ref. [91]). It has also been shown[92] that, when possible, numerical averaging based on small optimized supercells can give results considerably superior to the CPA. Furthermore, it should be pointed out that the CPA shows significant limitations when describing quantities where spatial correlations among different sites cannot be neglected. A discussion of the properties of CPA (its limits of validity, extensions, applications, etc.) is outside the scope of this work, and here we provide a short derivation which combines CPA and lattice DFT for quantum transport geometries. To this end, we must slightly modify the standard treatment[86–88] and adapt it to the case of a finite disordered sample in the presence of homogeneous semi-infinite contacts and within a lattice DFT context. We consider the case of diagonal disorder and specialize to a finite sample (chain of length L) of a random binary alloy, with species A and B and concentrations $c_A = N_A/L$ and $c_B = 1 - c_A$, respectively. In the quantum transport geometry we study, the chains are connected to noninteracting leads, as in Sec. V. For such chains, complete disorder averaging for a given concentration requires $\binom{L}{N_A}$ configurations, and already for $L = 14,15$ (as considered in this work) this number is rather large. In fact, performing time-dependent quantum transport calculations based on complete numerical averaging is computationally very demanding, and one is bound to use a much reduced (and incomplete) numerical sampling. This latter strategy is the one mainly adopted in the paper. To assess the scope of CPA, we limit ourselves to the ground state, when no bias is applied. Numerical results relative to this formulation are presented in Sec. VI B.

In matrix notation (in the site indexes) and in the absence of disorder and magnetic effects, the retarded one-body KS propagator for a chain connected to a left and a right lead can be written as

$$\hat{g}_{KS}(\omega) = \frac{1}{\omega \hat{1} - \hat{H}_{KS} - \hat{\sigma}_L(\omega) - \hat{\sigma}_R(\omega)}, \qquad (16)$$

where the matrix indexes of g_{KS} label the sites of the chain, $\hat{\sigma}_{L(R)}$ is the self-energy operator from the left (right) lead,[93] and $\hat{H}_{KS} = \hat{t} + \hat{v}_{KS}$ accounts for the kinetic and potential KS operators. In the presence of binary diagonal disorder $\hat{H} \rightarrow \hat{H}_{KS} + \hat{V}$, where $\hat{V} = \sum_i \epsilon_i \hat{n}_i$. Here, $\hat{n}_i = \sum_\sigma \hat{n}_{i\sigma}$. For ϵ_i, the probability distribution is $P(\epsilon_i) = c_A \delta(\epsilon_i - \epsilon_A) + (1 - c_A)\delta(\epsilon_i - \epsilon_B)$. The CPA provides a prescription to determine the effect of $\hat{V}$. In an exact fashion, we can equivalently write for the propagator $\langle G_{KS} \rangle$ averaged over all disorder configurations (the local dependence on ω is not shown):

$$\langle \hat{G}_{KS} \rangle = \hat{g}_{KS} + \hat{g}_{KS} \ \hat{\Sigma} \ \langle \hat{G}_{KS} \rangle, \qquad (17)$$

$$\langle \hat{G}_{KS} \rangle = \hat{g}_{KS} + \hat{g}_{KS} \ \langle \hat{\mathcal{T}}_V \rangle \ \hat{g}_{KS}. \qquad (18)$$

($\hat{\mathcal{T}}_V$ is the T matrix pertaining to a specific disorder configuration $\hat{V}$: $\hat{\mathcal{T}}_V = \hat{V} + \hat{V}\hat{g}_{KS}\hat{\mathcal{T}}_V$.) Inserting Eq. (18) in Eq. (17), and after some simple manipulations, we get

$$\hat{\Sigma} = \langle \hat{\mathcal{T}}_V \rangle [1 + \hat{g}_{KS}\langle \hat{\mathcal{T}}_V \rangle]^{-1}. \qquad (19)$$

In the CPA, the correlations among different scatterers are taken into account by assuming an effective medium for

which the single site scattering is zero on average. To see how, we start with a specific disorder configuration $\hat{V}$, for which $\hat{G}_{KS} = \hat{g}_{KS} + \hat{g}_{KS}\hat{V}\hat{G}_{KS}$. Then, we subtract from both sides the quantity $\hat{\Sigma}\hat{G}_{KS}$ (with $\hat{\Sigma}$ yet to be specified). This gives $(\hat{g}_{KS}^{-1} - \hat{\Sigma}) = 1 + (\hat{V} - \hat{\Sigma})\hat{G}_{KS}$ and, if we choose $(\hat{g}_{KS}^{-1} - \hat{\Sigma}) = \langle \hat{G}_{KS} \rangle^{-1}$, i.e., as in Eq. (17), we finally get

$$\hat{G}_{KS} = \langle \hat{G}_{KS} \rangle + \langle \hat{G}_{KS} \rangle (\hat{V} - \hat{\Sigma})\hat{G}_{KS}$$
$$= \langle \hat{G}_{KS} \rangle + \langle \hat{G}_{KS} \rangle \ (\hat{\mathcal{T}}_{V\Sigma}) \ \langle \hat{G}_{KS} \rangle, \qquad (20)$$

where the T matrix $\hat{\mathcal{T}}_{V\Sigma}$ pertains to the energy- and configuration-dependent potential $\hat{V} - \hat{\Sigma}$, i.e., $\hat{\mathcal{T}}_{V\Sigma} = (\hat{V} - \hat{\Sigma}) + (\hat{V} - \hat{\Sigma})\langle \hat{G}_{KS} \rangle \hat{\mathcal{T}}_{V\Sigma}$. Performing the average of Eq. (20) over different configurations, we note that it must be $\langle \hat{\mathcal{T}}_{V\Sigma} \rangle = 0$, the key exact condition for the T matrix.

The CPA makes two assumptions: (i) $\hat{\Sigma}$ is diagonal in the site-indexes, $\hat{\Sigma}_{ij}^{CPA} = \delta_{ij}\Sigma_i^{CPA}$, and so is the perturbation $\hat{V} - \hat{\Sigma}$; (ii) instead of $\langle \hat{\mathcal{T}}_{V\Sigma} \rangle = 0$, one imposes a simpler approximate constraint, i.e., that the average local T matrix at the ith site is zero:

$$\langle \mathsf{t}(i) \rangle = 0 = c_A \langle \mathsf{t}_A(i) \rangle + c_B \langle \mathsf{t}_B(i) \rangle, \qquad (21)$$

where

$$\mathsf{t}_{A(B)}(i) = \frac{\epsilon_{A(B)} - \Sigma_i^{CPA}}{1 - \langle \hat{G}_{KS} \rangle_{ii}[\epsilon_{A(B)} - \Sigma_i^{CPA}]}. \qquad (22)$$

In contrast to the usual treatments,[85–88] here all quantities in Eq. (22) depend on the site index, since our system exhibits no disorder in the leads. Very recently, and independently, a similar formulation has been provided in Ref. [94].

Inserting Eq. (22) in Eq. (21), and performing simple algebra, we arrive at an equation for Σ_i^{CPA}:

$$\Sigma_i^{CPA} - \epsilon_A = \frac{(1 - c_A)(\epsilon_B - \epsilon_A)}{1 - \langle \hat{G}_{KS} \rangle_{ii}[\epsilon_B - \Sigma_i^{CPA}]}. \qquad (23)$$

This equation must be solved for each site in the chain once the local propagator $\langle \hat{G}_{KS} \rangle_{ii}$ is known. The latter is, in turn, determined from Eq. (16), after the replacement $\hat{H}_{KS} \rightarrow \hat{H}_{KS} + \hat{\Sigma}^{CPA}$ is made, and after the dependence of $\hat{H}_{KS}$ on the densities has been taken into account via

$$n_i = - \int_{-\infty}^{\mu} \text{Im}\langle \hat{G}_{KS}(\omega + i0^+) \rangle_{ii} \frac{d\omega}{\pi}, \qquad (24)$$

with μ the chemical potential (here, as in the rest of the paper, we work at zero temperature). While it is certainly possible (and often necessary) to improve over the CPA,[95] in this work we aim at qualitative insight, and in Sec. VI B we present results obtained with the simple local formulation of CPA and the self-consistent set of equations Eqs. (16), (22), and (24).[96]

V. TIME-DEPENDENT QUANTUM TRANSPORT (TDQT) AND TDDFT

Theoretical approaches to quantum transport can be broadly grouped according to different criteria, e.g., if they are based on a steady-state or time-dependent formulations, if they use *ab initio* or model Hamiltonian methods, or according to which mathematical technique is employed: nonequilibrium-propagator, linear-response, wave-function-scattering, etc. Here we consider time-dependent quantum

transport (TDQT), which makes it possible to follow the system during its time evolution after a bias has been applied. In this way, steady-state, transient, and ac currents can all be considered on equal footing and, in the presence of dissipation, history dependence (memory effects) are also accounted for. A viable strategy to TDQT is to consider large but finite systems.[97] Via an initial spatial imbalance of particles, a quasi-steady-state current can be established. Recently this approach has also been used to describe bosonic and fermionic transport of ultracold atoms in 1D optical lattices.[98,99]

A different formulation, the one used here, considers a central region initially connected to semi-infinite leads.[100–102] This "contacted" approach has been used to introduce a TDDFT description of TDQT,[101,103] and the practical applicability of a TDDFT scheme has also been shown.[48] Furthermore, classical nuclear degrees of freedom have also been included in the approach.[104]

In a TDDFT approach to TDQT,[101,103] a key quantity is the XC potential. In Ref. 105, a combination of DMRG and lattice DFT was used to gain insight into the exact ground-state XC functionals for a correlated-electron model system coupled to external reservoirs. A comparison of lattice DFT and DMRG in transport has also been provided in Ref. 106, while a study of the role of spin in the XC potential can be found in Ref. 107 (for treatments based on ground-state current DFT for lattice models, see Refs. 108,109).

The effect of a discontinuity in v_{xc} in a TDDFT description of TDQT was examined within lattice TDDFT in the ALDA approximation.[74] Following the time evolution of a single Anderson impurity attached to two biased leads, a dynamical notion of the Coulomb blockade was then presented. This emerges also from a description based on time-dependent, bond-current DFT.[44] In Ref. 74, it was also suggested that for a single Anderson impurity, the exact v_{xc} is a sharp (at half filling) but smooth function of the density (the role of the discontinuity in v_{xc} has further been investigated in Ref. 110). Subsequently, a comparison between ALDA, tDMRG, and KBE for TDQT in lattice systems was presented in Ref. 111, showing that the ALDA can give accurate densities but overestimated currents, due to the neglect of nonlocal effects in the leads. (A characterization of the time-dependent, exact XC potential in finite-size quantum transport geometries was given in Ref. 112.) Finally, we mention that, recently, different research groups[58,75,113] independently pointed out that suitable XC potentials permit a (TD)DFT description of the Kondo effect and also examined in detail the broadening of the derivative discontinuity of the XC potential.[58,75–77]

A. Time evolution for quantum transport

The time-dependent scheme used in this work is the one developed in Ref. 48 and, as in Ref. 74, interactions in the central region are treated via an ALDA from the Bethe ansatz.[41] For disordered systems, where large central regions and configuration averages may be needed, such an algorithm may be computationally expensive. As described in Sec. V B, a convenient way to enhance its numerical efficiency is to use the Lanczos recursion for time evolution[114] (for a quick introduction to the Lanczos technique, see Appendix A).

We start with a concise description of the original algorithm,[48] as background to our Lanczos-adapted scheme, and we specialize to 1D geometries. The notation in this and the next section is closer to the one in Ref. 48 and thus differs from that in the rest of our paper.

The Hamiltonian we consider is $\mathbf{H}^{tot}(t) = \mathbf{H}_{el} + \mathbf{\Xi}(t)$, where $\mathbf{\Xi}(t)$ is the external perturbation. In a TDDFT approach, the initial, ground state is a single Slater determinant $|\Psi_g\rangle$. It is useful to divide the (1D) space into three regions. With s the site label, we have the region L [corresponding to the left lead, with $s \leqslant -(M+2)$], the central region C (with $|s| \leqslant M+1$, i.e., the device region contains $2M+3$ sites), and the region R [corresponding to right lead, with $s \geqslant (M+2)$]. The general structure of any bound, extended, or resonant one-particle eigenstate ψ in the Slater determinant $|\Psi_g\rangle$ can be written as

$$\psi(s) = \begin{cases} L_+ e^{-ik_l s} + L_- e^{ik_l s}, & s \leqslant -M-2, \\ \psi(s), & |s| \leqslant M+1, \\ R_+ e^{ik_r s} + R_- e^{-ik_r s}, & s \geqslant M+2. \end{cases} \quad (25)$$

To describe quantum transport, one needs to evolve in time the ground-state configuration $|\Psi_g\rangle$, i.e., each one of the single particle eigenstates ψ above. Introducing the projection operators $\mathbf{P}_{L,C,R}$ (for example, $\mathbf{P}_L = \sum_{s \in L} |s\rangle\langle s|$), we can write ($\beta = L, C, R$), for the generic single-particle state,

$$|\psi\rangle = \sum_\beta |\psi_\beta\rangle, \quad |\psi_\beta\rangle = \mathbf{P}_\beta |\psi\rangle. \quad (26)$$

In the same way, we can project the Hamiltonian in the different regions

$$\mathbf{H} = \sum_{\beta\beta'} \mathbf{H}_{\beta\beta'}, \quad \mathbf{H}_{\beta\beta'} \equiv \mathbf{P}_\beta \mathbf{H} \mathbf{P}_{\beta'}. \quad (27)$$

Separating the contribution from the leads in $\mathbf{\Xi}$, the set of one-particle equations becomes

$$i\frac{\mathrm{d}}{\mathrm{d}t}|\psi(t)\rangle = [\mathbf{H}(t) + \mathbf{\Xi}_{\text{leads}}(t)]|\psi(t)\rangle, \quad (28)$$

with $\mathbf{H}(t) = \mathbf{H}_{el} + \mathbf{\Xi}_{CC}(t)$, where $\mathbf{H}_{el}$ is the electron one-particle Hamiltonian and $\mathbf{\Xi}_{CC}(t)$ is the external potential projected in the central region C. Assuming metallic electrodes,

$$\mathbf{\Xi}_{\text{leads}}(t) = \begin{cases} \delta_{s,s'} \Xi_L(t), & s \leqslant -M-2, \\ 0, & s \leqslant |M+1|, \\ \delta_{s,s'} \Xi_R(t), & s \geqslant M+2. \end{cases} \quad (29)$$

In the numerical time propagation, the time is discretized: $t_m = 2m\delta$, where δ is the time step, m is an integer, and the explicit prefactor 2 is introduced for convenience in the formulas. In Ref. 48, the one-particle eigenstates are propagated from t_m to t_{m+1} using a generalized Crank-Nicholson scheme. For the time evolution of each one of the one-particle states in $|\Psi_g\rangle$,

one gets[48]

$$(1 + i\delta\mathbf{H}^{(m)})\frac{1 + i\frac{\delta}{2}\mathbf{\Xi}_{\text{leads}}^{(m)}}{1 - i\frac{\delta}{2}\mathbf{\Xi}_{\text{leads}}^{(m)}}|\psi^{(m+1)}\rangle$$

$$= (1 - i\delta\mathbf{H}^{(m)})\frac{1 - i\frac{\delta}{2}\mathbf{\Xi}_{\text{leads}}^{(m)}}{1 + i\frac{\delta}{2}\mathbf{\Xi}_{\text{leads}}^{(m)}}|\psi^{(m)}\rangle, \quad (30)$$

where $|\psi^m\rangle \equiv |\psi(t_m)\rangle$ and

$$\mathbf{H}^{(m)} = \mathbf{H}_{\text{el}} + \tfrac{1}{2}\left[\mathbf{\Xi}_{CC}(t_{m+1}) + \mathbf{\Xi}_{CC}(t_m)\right], \quad (31)$$

$$\mathbf{\Xi}_{\text{leads}}^{(m)} = \tfrac{1}{2}[\mathbf{\Xi}_{\text{leads}}(t_{m+1}) + \mathbf{\Xi}_{\text{leads}}(t_m)]. \quad (32)$$

Using Eqs. (26) and (27), and after some algebra, the closed equation for the time evolution in the central region is

$$|\psi_C^{(n+1)}\rangle = \frac{\mathbf{1}_C - i\delta\mathbf{H}_{\text{eff}}^{(n)}}{\mathbf{1}_C + i\delta\mathbf{H}_{\text{eff}}^{(n)}}|\psi_C^{(n)}\rangle$$

$$- 2i\delta\sum_{\alpha=L,R}\frac{\Omega_\alpha^{(n)}}{w_\alpha^{(n)}}\left(|\gamma_\alpha^{(n)}\rangle + |\zeta_\alpha^{(n)}\rangle\right), \quad (33)$$

where

$$w_\alpha^{(n)} = \frac{1 - i\frac{\delta}{2}\Xi_\alpha^{(n)}}{1 + i\frac{\delta}{2}\Xi_\alpha^{(n)}}, \quad (34)$$

$$\Omega_\alpha^{(n)} = \prod_{j=0}^{n}\left[w_\alpha^{(j)}\right]^2, \quad (35)$$

and

$$\mathbf{H}_{\text{eff}}^{(n)} = \mathbf{H}_{CC}^{(n)} - i\delta\sum_{\alpha=L,R}\mathbf{H}_{C\alpha}\frac{1}{\mathbf{1}_\alpha + i\delta\mathbf{H}_{\alpha\alpha}}\mathbf{H}_{\alpha C}$$

$$= \mathbf{H}_{CC}^{(n)} - i\delta\sum_{\alpha=L,R}\mathbf{B}_\alpha^{(0)}. \quad (36)$$

The $\mathbf{B}_\alpha^{(0)}$ matrices have only one nonzero element,

$$\left[\mathbf{B}_\alpha^{(0)}\right]_{s,s'} = b^{(0)}\begin{cases}\delta_{s,-M-1}\delta_{s',-M-1}, & \alpha = L,\\ \delta_{s,M+1}\delta_{s',M+1}, & \alpha = R,\end{cases} \quad (37)$$

with $b^{(0)} = \frac{-1+\sqrt{1+4\delta^2 V^2}}{2\delta^2}$ and V the hopping parameter in the leads. The expressions for the source state $|\gamma_\alpha^{(n)}\rangle$ and the memory state $|\zeta_\alpha^{(n)}\rangle$ are[48]:

$$\left|\zeta_\alpha^{(n)}\right\rangle = Z_\alpha^{(n)}\frac{1}{\mathbf{1}_C + i\delta\mathbf{H}_{\text{eff}}^{(n)}}|u_\alpha\rangle, \quad (38)$$

$$\left|\gamma_\alpha^{(n)}\right\rangle = G_\alpha^{(n)}\frac{1}{\mathbf{1}_C + i\delta\mathbf{H}_{\text{eff}}^{(n)}}|u_\alpha\rangle, \quad (39)$$

where $|u_\alpha\rangle$ is a unit vector such that

$$\langle s|u_\alpha\rangle = \begin{cases}\delta_{s,-M-1}, & \alpha = L,\\ \delta_{s,M+1}, & \alpha = R.\end{cases} \quad (40)$$

The scalar quantities $Z_\alpha^{(n)}$ and $G_\alpha^{(n)}$, $\alpha = L, R$ are given by

$$Z_\alpha^{(n)} = \frac{\delta}{2i}\sum_{j=0}^{n-1}\frac{w_\alpha^{(j)}}{\Omega_\alpha^{(j)}}(b^{(n-j)} + b^{(n-j-1)})$$

$$\times\left(\langle u_\alpha|\psi_C^{(j+1)}\rangle + \langle u_\alpha|\psi_C^{(j)}\rangle\right), \quad (41)$$

$$G_\alpha^{(n)} = (\alpha_+ e^{iz_\alpha(M+2)} + \alpha_- e^{-iz_\alpha(M+2)})V\frac{(1 - 2i\delta\cos(z_\alpha))^n}{(1 - 2i\delta\cos(z_\alpha))^{n+1}}$$

$$+ (\alpha_+ e^{iz_\alpha(M+1)} + \alpha_- e^{-iz_\alpha(M+1)})$$

$$\times i\delta\sum_{j=0}^{n}\frac{(1 - 2i\delta\cos(z_\alpha))^{n-j}}{(1 - 2i\delta\cos(z_\alpha))^{n+1-j}}(b^{(j)} + b^{(j+1)}) \quad (42)$$

and $z_\alpha = k_l$ for $\alpha = L$, while $z_\alpha = k_r$ for $\alpha = R$. For $n \geqslant 2$, the quantities $b^{(n)}$ in Eqs. (41) and (42) are obtained by recursion,

$$b^{(n)} = \frac{b^{(1)}b^{(n-1)}}{b^{(0)}} - \delta^2\frac{b^{(0)}b^{(n-2)}}{1 + 2\delta^2 b^{(0)}}$$

$$- \delta^2\sum_{j=1}^{n-1}\frac{(b^{(j)} + b^{(j-1)} + b^{(j-2)})b^{(n-2-j)}}{1 + 2\delta^2 b^{(0)}}, \quad (43)$$

and $b^{(n<0)} = 0, b^{(1)} = \frac{1-2\delta^2 b^{(0)}}{1+2\delta^2 b^{(0)}}b^{(0)}$ and $b^{(0)}$ the same as in Eq. (37).

B. Lanczos-adapted algorithm

The basic idea behind the algorithm discussed in the previous Section is to discretize the time axis via the Crank-Nicholson algorithm *before* performing the partitioning in L, C, and R regions.[48] One could think of doing the same using the Lanczos algorithm for the time propagation[114] (the method is quickly reviewed in Appendix A); however, noncommuting parts of the Hamiltonian would appear in the exponent this time, rendering formal manipulations more involved. Here, we consider a simple shortcut that, while improving the numerical efficiency of the algorithm of Sec. V A, has the same degree of accuracy (i.e., it is second order in δ) but avoids working with the Lanczos scheme before the partitioning.[115] Looking at Eq. (33), we notice that the explicit action of $\mathbf{H}_{\text{eff}}^{(n)}$ occurs in two specific terms:

$$|\chi_1\rangle = \frac{\mathbf{1}_C - i\delta\mathbf{H}_{\text{eff}}^{(n)}}{\mathbf{1}_C + i\delta\mathbf{H}_{\text{eff}}^{(n)}}|\psi_C^{(n)}\rangle, \quad (44)$$

$$|\chi_2\rangle = \frac{1}{\mathbf{1}_C + i\delta\mathbf{H}_{\text{eff}}^{(n)}}|u_\alpha\rangle, \quad (45)$$

where $|\chi_1\rangle$ is the contribution to $|\psi_C^{(n+1)}\rangle$ from the central region and $|\chi_2\rangle$ enters the expressions for the source and memory states. For $|\chi_1\rangle$, since $\delta \to 0$, one can write, up to order two in δ

$$|\chi_1\rangle = \frac{\mathbf{1}_C - i\delta\mathbf{H}_{\text{eff}}^{(n)}}{\mathbf{1}_C + i\delta\mathbf{H}_{\text{eff}}^{(n)}}|\psi_C^{(n)}\rangle \approx e^{-2i\delta\mathbf{H}_{\text{eff}}^{(n)}}|\psi_C^{(n)}\rangle. \quad (46)$$

For the case of $|\chi_2\rangle$, we define the following quantities:

$$\Delta_\pm = \frac{1 \pm \sqrt{3}}{2}\delta, \quad (47)$$

which permit to rewrite $|\chi_2\rangle$ as

$$|\chi_2\rangle = \left[-1 + e^{-i\mathbf{H}_{\text{eff}}^{(n)}\Delta_+} + e^{-i\mathbf{H}_{\text{eff}}^{(n)}\Delta_-}\right]|u_\alpha\rangle + O(\delta^3). \quad (48)$$

If necessary, one can go to higher orders, by imposing that $(1 + \delta x)^{-1} = A + \sum_k e^{a_k\delta x}$ and finding the coefficients $A, \{a_k\}$ by comparison of the two expressions order by order in δ (in general, the $\{a_k\}$ will be complex). We note that

the same Lanczos sequence of basis vectors is required for both exponentials in Eq. (48). All terms which appear in the propagation scheme of Sec. V A and that involve $\mathbf{H}_{\text{eff}}^{(n)}$, have been re-expressed in terms of exponentials, so that Lanczos propagation can be used; finally, since $\mathbf{H}_{\text{eff}}^{(n)}$ is complex, Eq. (36), it is convenient to split the exponentials; for small δ,

$$e^{-2i\delta\mathbf{H}_{\text{eff}}^{(n)}} \approx e^{-\delta^2 \sum_\alpha \boldsymbol{B}_\alpha^{(0)}} e^{-2i\delta\mathbf{H}_{CC}^{(n)}} e^{-\delta^2 \sum_\alpha \boldsymbol{B}_\alpha^{(0)}}, \qquad (49)$$

$$e^{-i\Delta_\pm\mathbf{H}_{\text{eff}}^{(n)}} \approx e^{-\frac{\delta}{2}\Delta_\pm \sum_\alpha \boldsymbol{B}_\alpha^{(0)}} e^{-i\Delta_\pm\mathbf{H}_{CC}^{(n)}} e^{-\frac{\delta}{2}\Delta_\pm \sum_\alpha \boldsymbol{B}_\alpha^{(0)}}. \qquad (50)$$

For the 1D case, the advantage is immediate: The $\boldsymbol{B}_\alpha^{(0)}$ in Eq. (37) have only one nonvanishing entry and the outer exponentials in Eqs. (49) and (50) reduce to scalars. We expect that the splitting will still provide a simplification in the 3D case. To summarize, on increasing the size of the central region, our Lanczos adapted scheme becomes highly convenient, potentially a significant advantage when dealing with disordered and large samples.

VI. RESULTS

Recently, a nonperturbative study of finite Anderson-Hubbard chains has been performed in terms of density matrix renormalization group and a real-space version of DMFT.[116] Using different indicators of delocalization, such as the geometrically averaged LDOS and the IPR, the main outcome of such nonperturbative calculations was a clear indication of a tendency to delocalization in a range of U, W values in the ground state of these chains. Can a similar behavior be observed in shorter chains contacted to semi-infinite leads? To address this issue, we present here ground-state and dynamical results for short, isolated/contacted disordered, and interacting chains. No spin-effects are considered; i.e., the systems are spin compensated, and all applied potentials are spin independent. The quantities we analyze are the on-site particle density, the bond current, and the IPR. In general, we consider box disorder, with on-site energies ϵ_l uniformly distributed in the interval $[-W/2, W/2]$. In this case, configuration averages will be done over a finite number of configurations. However, we used binary disorder to discuss the IPR (Sec. VI A) and the CPA (Sec. VI B), since, for short chains, exact averaging can be done with a manageable number of configurations. Further details of each set/type of calculation are provided in the respective sections.

A. Changing the definition of the IPR

To analyze our definition of IPR, Eq. (15), we find it convenient to consider binary (rather than uniform) disorder in a noninteracting chain of $L = 14$ sites. For binary disorder, choosing L small and even makes it possible (i) to consider exactly the $A_{50}B_{50}$ alloy concentration and (ii) to perform disorder averages exactly. The chain can be isolated or contacted to two 1D leads (one at each end of the chain); the leads can be finite or semi-infinite (their length is denoted by N_{ld}). The total number of sites in the system is thus $M = L + 2N_{ld}$. We wish at this point to make a short technical digression on the numerical calculation of the IPR. For the energy-dependent IPR, we need the local density of states

(LDOS) at site(s) i:

$$n_i(\omega) = \frac{\gamma}{\pi} \sum_\lambda \frac{|\langle\lambda|i\rangle|^2}{(\omega - E_\lambda)^2 + \gamma^2}, \qquad (51)$$

where λ labels the one-particle eigenstates $|\lambda\rangle$ and eigenvalues E_λ of the system. For infinite systems, Eq. (51) is not usable directly, and one resorts to Green's functions [see Eq. (16) in Sec. IV B]. For finite systems, one can, e.g., use recursion techniques,[82] or, as done in this section, perform a direct diagonalization of the disordered Hamiltonian. However, if the IPR must be determined in a range of energies (i.e., for several ω values), already for moderate system sizes M, the λ and i sums in Eqs. (14), (15), and (51) become computationally expensive. In Appendix B, we present a technique which makes it possible to perform such nested summations in a rather efficient way.

Results for the IPR according to the two definitions ζ_2, Eq. (14), and ζ_3, Eq. (15), are shown in Fig. 1 (hereafter, ζ_2 and ζ_3 will be renamed IPR_{system} and IPR_C, respectively). Calculations with IPR_{system} are reported in panels (a), (c), and (e). In all three panels, we see that on increasing the size N_{ld} of the (finite) leads, $IPR_{\text{system}}(\omega)$ gets quickly reduced in the region $|\omega| \leqslant 2$, i.e., for the energy range for the extended states in the system (results for larger N_{ld}, not shown, confirm this trend). Outside the band region, the decay of $IPR_{\text{system}}(\omega)$ on increasing N_{ld} is much slower, and our numerical evidence, together with arguments based on the large W limit, shows that for larger N_{ld}, $IPR_{\text{system}}(\omega)$ vanishes everywhere for $|\omega| \geqslant 2$ except at the energies of the localized states, where it takes the corresponding IPR value. Thus, irrespective of the disorder strength in the finite chain, in the limit of semi-infinite leads, IPR_{system} indicates delocalization for $|\omega| \leqslant 2$. However, for a large disorder, the chain becomes disconnected from the leads, and this is missed in the vanishing IPR_{system}, which simply reflects almost everywhere the delocalized states in the disconnected leads (as in most quantum transport treatments, the leads are assumed to be homogeneous and noninteracting).

In panels (b), (d), and (f) of Fig. 1, we show results for $IPR_C(\omega)$; in this case, on increasing N_{ld}, the IPR tends to a finite value (the asymptotic value for when $N_{ld} \to \infty$), which better reflects the fact that the localization in some region of the system affects the system as a whole (we have also verified that on increasing W, IPR_C increases). Being a local quantity, IPR_C obviously depends on the size and the details of the chain.

When interactions among particles are taken into account, there is another point that is necessary to examine. This aspect is specific to our approach to quantum transport, where interactions are described within lattice (TD)DFT. Since the KS system is just a fictitious system apt to reproduce the true interacting density, a frequency-dependent IPR of the KS system has actually little physical meaning. Thus, our final proposed definition of IPR is

$$IPR_C^{KS} = \sum_{i \in C} \left[n_i^{KS}\right]^2 \Big/ \left[\sum_{i \in C} n_i^{KS}\right]^2. \qquad (52)$$

Equation (52), which makes use of the actual particle density, can also be used in the interacting and time-dependent cases and thus is both conceptually and operationally well defined
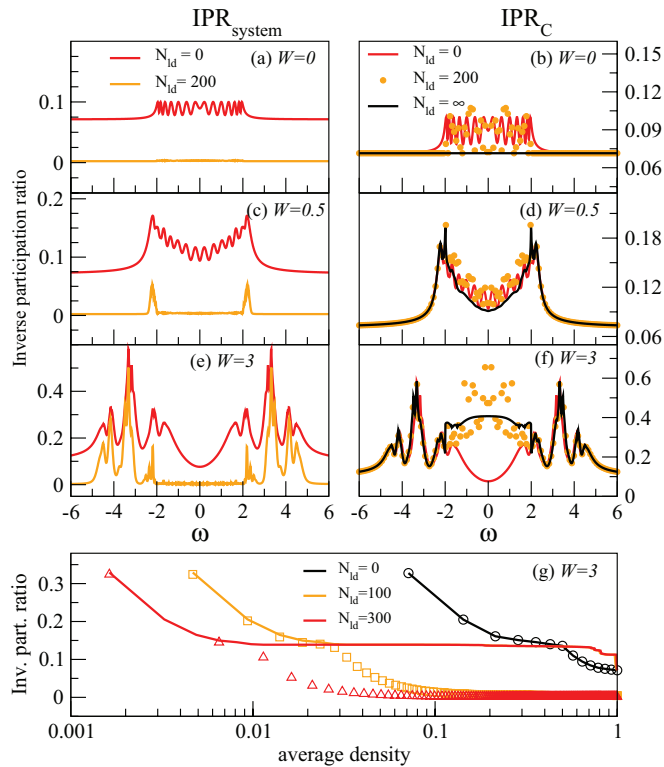
FIG. 1. (Color online) Disorder-averaged IPR (see main text for the definitions) for a $A_{50}B_{50}$, noninteracting binary-alloy chain C with $L = 14$ sites, contacted to infinite/finite leads. Complete disorder averages were performed over $\binom{L}{N_A} = 3432$ configurations. (a)–(f) Energy-dependent IPR [Eqs. (14) and (15)]. Top-to-bottom panels show cases with increasing disorder strength W, while left (right) panels show results for an IPR evaluated by summing over the entire system (only over the chain C), as in Eq. (14) [Eq. (15)]. The color/symbol coding in panel (a) [(b)], also applies to panels (c),(e) [(d),(f)]. In panels (a),(c),(e), $IPR_{\text{system}}(\omega)$ for infinite leads ($N_{ld} \to \infty$) is not shown. In (a)–(f), all curves were obtained with a small Lorentzian broadening γ, to have a minimum accuracy of 10^{-4} for $IPR_C(\omega)$ when $N_{ld} \to \infty$ [black curves in panels (b),(d),(f)]. Panel (g): IPR_C^{KS} obtained by summing only over the central region [Eq. (52), solid lines] or over the entire system (circle, square, and diamond symbols). Results are shown as function of the average density/spin-channel and for three lead lengths N_{ld}.

within (TD)DFT. IPR_C^{KS} is also sensitive to localization and tends to a finite value when the size of the leads tend to infinity, as shown in Fig. 1. In panel (g), we show IPR_C^{KS} for leads of different lengths, as a function of the average density in the system $(\sum_{i=1}^{M} n_i)/M$ (the average density is varied by changing the number of occupied one-particle eigenstates of the system with $L + 2N_{ld}$ sites).

We see that, on increasing the lead length, IPR_C^{KS} tends to a finite value on a progressively large interval of (average) densities (on the scale of the figure, already for $N_{ld} = 100,300$, the corresponding IPRs coincide for $n \gtrsim 0.1$). We also show the density-dependent IPR when extending the sum to the entire system. In this case, on increasing N_{ld}, the IPR tends to zero on an increasingly larger density region.

How to establish a rigorous link between localization and IPR_C^{KS} appears to be a nontrivial task. However, a heuristic argument can be the following: For uniform density, $IPR_C^{KS} = 1/L$ while, if the sums in Eq. (52) are extended to all the $M = L + 2N_{ld}$ sites, then $IPR = 1/M$, i.e., much smaller than $1/L$. However, IPR_C^{KS} is a measure of the spread of the density values n_i, and when states with (more) localized character contribute to n_i, then the variance of n_i within the chain C makes $IPR_C^{KS} > 1/L$, which is thus suggestive of localization. On the other hand, the contribution from C become less relevant when the sum in Eq. (52) is extended to all M sites, except for low densities (where states with lower energy, and thus more localized behavior, are those mostly contributing). Thus we expect that for a given W, IPR_C^{KS} will be considerably larger than $1/L$ at low density, will then decrease as the density increases (while still being larger than $1/L$) and will eventually become $1/L$ when the density/spin-channel reaches 1 (i.e., the number of particle equals $2M$). When the sum is extended to all M sites, extended states become relevant already at rather low density, and the IPR tends tend much faster to $1/M$. This behavior persists when we introduce interactions at the DFT-LDA level, and is consistent with localization trends as displayed by the behavior of the currents (see Sec. VI C below).

The results in panels (a)–(g) are in terms of *arithmetic* averages over the disorder configurations. For IPR_C^{KS} (which will be used in the rest of the paper), we have also considered *geometric* averages over disorder, with results almost identical to those in panel (g). This is discussed in detail in Sec. VI D. Our emphasis in this and the following sections is on the IPR as an indicator of localization. One could consider other possibilities as well. For example, the linear conductance could be examined, since this quantity is expected to decay exponentially in the localized regime. (In the spirit of this work, the conductance should be calculated in the KS framework.)

The topic of KS conductances in lattice models has been addressed in several works.[58,75–77,105,112,113,117–119] These studies show that for single-channel molecular junctions, and at zero temperature, the exactness of the KS conductance is ensured by the Friedel's sum rule. At the same time, the same works (see especially Refs. [117,118]) point out that, in general, the connection between KS and exact conductance is only approximate for multichannel junctions. Still, even as an approximate quantity, the KS conductance could be investigated as an indicator for systems dominated by direct Coulomb interactions, or when conduction is prevalently due to a single channel (however, in disordered systems, the latter, limiting situation cannot be easily assessed beforehand).

Finally, one might also try employing the TDDFT frequency-dependent density response to extract a frequency-dependent IPR. This could be an alternative to studying disorder via nonequilibrium Green's functions, where obtaining a frequency-dependent IPR is straightforward. These prescriptions, and an analysis of the KS conductance are, however, deferred to future work.

To summarize, while not arguing that our definition of IPR is an optimal or unique indicator of localization in quantum transport geometries,[120] in our simulations we used Eq. (52) as a viable prescription when using TDDFT for time-dependent quantum transport.

B. CPA-DFT for short chains attached to leads

For a short disordered chain connected to homogeneous leads, a treatment based on the single-site CPA amounts to introducing a complex, energy- and site-dependent self-energy. Numerically, this CPA procedure is quite convenient, since it amounts to solving self-consistently a set of equations. However, how accurate is the CPA for the kind of (quantum-transport) geometries considered in this paper? To answer this question, we have considered a disordered chain with $L = 14$ sites in the absence of particle-particle interactions ($U = 0$). The chain represents a $A_{25}B_{75}$ and a $A_{50}B_{50}$ system; i.e., in the notation of Sec. IV B, $c_A = 0.5$ and $c_A = 0.25$, with $c_B = 1 - c_A$. We considered two disorder strengths, i.e., $W = \epsilon_A = -\epsilon_B$ equal to 0.5 and 1.0. The quantity that we intend to examine is the KS average LDOS, defined as $\langle d(\omega) \rangle_{ii} = -\pi^{-1}\mathrm{Im}\langle \hat{G}_{KS}(\omega) \rangle_{ii}$ (i labels the ith site in the chain), with $\langle \hat{G}_{KS}(\omega) \rangle$ obtained as described in Sec. IV B. Strictly speaking, the LDOS is not accessible to ground-state DFT; nevertheless, we think it is instructive to look at the KS LDOS in the framework of DFT, to compare CPA versus exact disorder averaging when interactions are present.

For numerical convenience, the calculations were performed with an additional small Lorentzian broadening. The results for $U = 0$ are presented in Fig. 2 (see the figure caption for additional details). In each panel, the LDOSs are obtained with both exact averages, summing over $\binom{14}{7} = 3432$ configurations, and with the CPA. Furthermore, in each panel, we show LDOSs at sites adjacent to the leads (labeled as "edge") and at a site in the center of the chain (labeled as "middle"). Irrespective of the strength of the disorder, the results show that, overall, the CPA (at least in this simple single-site formulation) provides a fair account of the role of the disorder, but much of the sharp structures in the exact curves are washed out. For example, for $W = 1$, for $\omega \gtrsim 1$, we note a significant depression of the exact LDOS, which is completely missed by the CPA. More in general, the sharp structures (bound states) outside the continuum are removed by the CPA. This can have consequences in the long-time limit of quantum transport: For pure systems, bound states in the final-state KS Hamiltonian can give rise to steady-state oscillations,[122,123] but, due to disorder as treated in the CPA, such long-lived oscillations are expected to be damped.[124] The situation is less clear for the exactly averaged LDOS: One can expect a self-averaging of the current and/or density oscillations when the chain increases in size. However, for short chains, and for the simple type of binary, on-site disorder considered here, (small) long-time oscillations could persist. It can be of interest to see to what extent this behavior is modified in the presence of interparticle interactions. In Fig. 3, the LDOSs for $U = 0$ and $U = 3$ are plotted for a chain with and without disorder. In the main panel, results were obtained in terms of arithmetic averages, while geometrical averages were used for the curves in the inset panel. We postpone a discussion of the latter to Sec. VI D and confine the analysis here to the main panel, i.e., to arithmetic averages. The curves for $U = 3$ were obtained with lattice DFT in the LDA. Starting with the $W = 0$ case, we note that an important effect of the interactions comprises resonant structures at the top of the band ($\omega \gtrsim 2$, blue curve). The addition of disorder within a
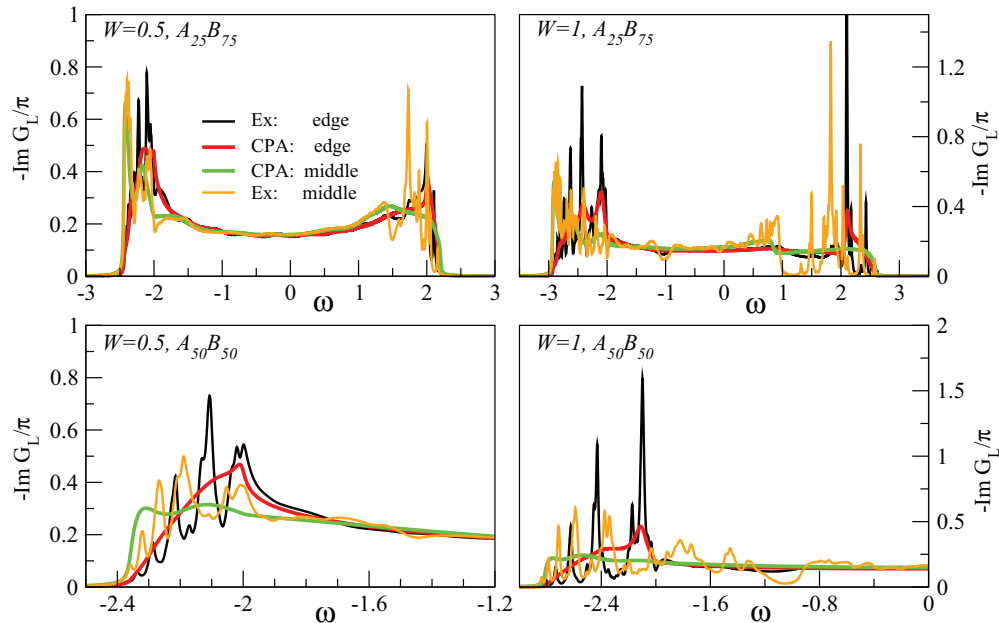

FIG. 2. (Color online) CPA versus exact averaging for a chain with 14 sites connected to two semi-infinite homogenous leads, with transparent boundary conditions. The meaning of each curve is given by the color coding in the top-left panel. In the legend, *Ex* means complete numerical averaging. The density of states for the leads is nonzero in the interval $[-2,2]$ and the chemical potential $\mu = 0$ in the leads (half filling). In each panel, the average LDOS is presented for middle and edge sites (see main text) and as obtained with CPA (red and green curves) and exactly (black and orange curves), and two strengths of disorder W are considered. For the $A_{50}B_{50}$ systems (bottom panels) all curves are symmetric with respect to $\omega = 0$. For $W = 1$, the maxima of some of the sharp peaks at the band edges are outside the scale shown in the figure.
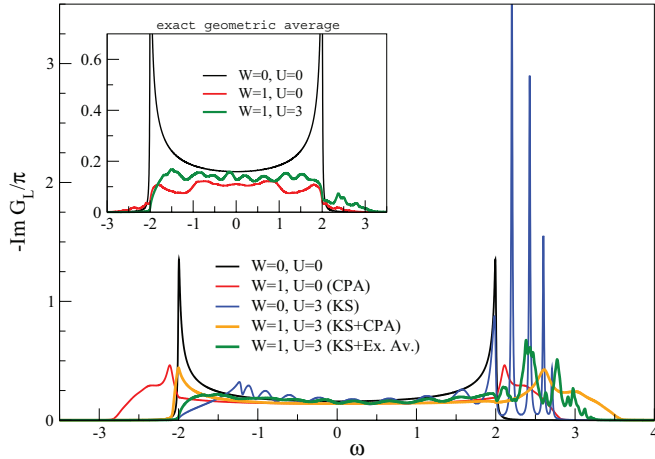
FIG. 3. (Color online) LDOS at an edge site for a disordered ($A_{50}B_{50}$) and noninteracting/interacting 14-site chain contacted to two homogenous 1D leads at half filling. The other system parameters are as in Fig. 2. For both the main and the inset panels, the interactions are treated within a KS scheme. In the main panel, *Ex. Av.* means complete, numerical arithmetical averaging. In the inset, the curves were obtained via complete numerical geometrical averages.

CPA treatment has an overall effect similar to what observed in Fig. 2, namely both the KS sharp structures are dramatically smoothed in the KS + CPA LDOSs (orange curve).[125] As for the noninteracting case [for reference, the CPA result for $U = 0$ is also shown (red curve)], the use of the CPA could considerably affect the long-time behavior of densities and currents induced by a bias. This is because the sharp structures due to the interaction in the DFT-LDA (that could induce long time limit oscillations in an ALDA treatment) are smoothed by the CPA. For the exactly averaged interacting LDOS, we equally observe a clear broadening/reduction of the split-off KS structures, albeit less pronounced than in the CPA-KS curve. Due to the artificial broadening we introduced in our calculations, it cannot be excluded that for short chains the density and current oscillations would stay long lived. The results shown here were obtained from the initial state Hamiltonian. However, similar split-off structures are present in the case of the final-state Hamiltonian, and the actual oscillations, independently from the presence of disorder, would likely be absent if memory effects were taken into consideration.[111]

C. (TD)DFT results for short chains attached to leads: Static, transient, and steady-state regimes

In general, for disordered chains attached to semi-infinite leads, an exact numerical treatment analogous to the one which we will discuss in Sec. VI E is not available. In this case, two suitable methods are (TD)DFT and the Green's functions technique. These two methods are both exact in principle but, in practice, the many-body self-energy in a propagator approach and v_{xc} in TDDFT are not known exactly, and approximations are in order. Here we consider a TDDFT description, as presented earlier in the paper. Our only (but important) approximation will be the use of a local density approximation (LDA) in the ground state, and its adiabatic

TABLE I. Inverse participation ratio in the ground state. Arithmetic disorder averages are performed over 50 configurations.

	n	$U = 0$	$U = 2$	$U = 4$
$W = 0$	1.0	$0.0\overline{6}$	0.067	0.067
	0.5	$0.0\overline{6}$	0.067	0.067
$W = 1$	1.0	0.068	0.067	0.067
	0.5	0.072	0.071	0.069
$W = 3$	1.0	0.078	0.073	0.072
	0.5	0.109	0.096	0.09

counterpart (ALDA) during the dynamics. The quality of these approximations in the present contexts is briefly discussed at the end of this section.

1. In equilibrium: The inverse participation ratio

We begin studying the system in equilibrium. The central region is a chain of $L = 15$ sites. We consider three strengths of disorder in the chain, $W = 0, 1, 3$ and three values of the interaction, $U = 0, 2, 4$. Both U and W are given in units of the hopping parameter. In Table I, we show the results for the configuration-averaged IPR for different densities $n = n_\uparrow + n_\downarrow$ in the leads (quarter- and half-filling cases). The average was performed over 50 configurations. As discussed in Sec. IV A, the IPR is calculated in terms of the KS densities in the central region [Eq. (52)].

For $U = W = 0$, the system is homogenous, and we have only fully delocalized states and, since $L = 15$, we get an $IPR_C = L^{-1} = 0.0\overline{6}$. Accordingly, values larger than $0.0\overline{6}$ would denote a tendency to localization. This is what we observe on moving to larger W values, while keeping $U = 0$: Localization is maximal for $W = 3$, both at quarter and half filling (however, the degree of localization is different for the two fillings). A similar dependence of the IPR on W is observed for $U = 2$ and $U = 4$. However, a different behavior is noted when changing U at a fixed W (i.e., moving horizontally in the table). We see that the IPR stays approximatively constant at low W but, for larger disorder, the IPR decreases on increasing U (see especially the case of $W = 3$). That is, increasing U decreases localization, a manifestation of the competing behavior of interactions and disorder. This has been noted before for finite samples (e.g., in terms of exact diagonalization[121] or DMRG calculations[116]). When W and U become both very large, calculations as in Refs. 121 and 116 suggest that localization prevails. From our results, this should happen at U values larger than those in the table (e.g., for $W = 3$, at $U > 4$). However, for such interaction strengths, the shortcomings of the Bethe ansatz LDA can become particularly severe.[126] Nevertheless, it is quite interesting that a competing regime between disorder and interactions is accounted for within our lattice DFT-LDA approach, and with disorder occurring only in a subregion of the system.

2. Time-dependent densities

This behavior should also manifest in the dynamical properties of the chain. To see this, we studied the time evolution of the system, after the application of a bias in the leads. Our choice was to apply the bias only in the left lead
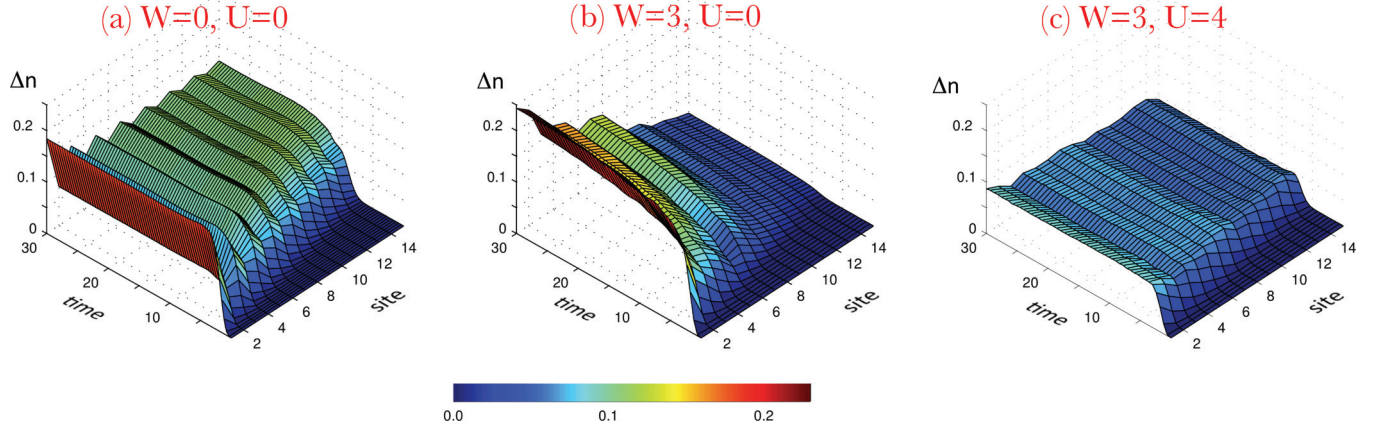
FIG. 4. (Color online) Difference between nonequilibrium and ground-state (initial) densities, in a chain with $L = 15, n = 1$, and box disorder W, when a bias $b_S(t)$ is applied in one of the two leads, and $b_0 = 1.5$ [see Eq. (53)]. The maximum evolution time is $T_{\max} = 30$, in units of the inverse hopping parameter in the chain. Arithmetical disorder averaging is performed over 50 configurations.

[i.e., at all times, $b_D(\tau) = 0$; see Eq. (1)], with the following time dependence:

$$b_S(\tau) = \begin{cases} b_0\left[1 + \cos\pi\left(1 + \frac{\tau}{T}\right)\right]/2, & 0 \leqslant \tau \leqslant T, \\ b_0, & \tau > T, \end{cases} \quad (53)$$

where $T = 3$ (all time quantities are expressed in units of the reciprocal chain hopping). This choice of T is somewhat arbitrary, but in this way the effect of $b_S(\tau)$ is rather gradual, a situation expected to be favorable to the use of an ALDA based on the Bethe ansatz for the 1D Hubbard model. Our time-dependent results were obtained with propagation time steps of either $\Delta\tau = 0.0025$ or $\Delta\tau = 0.0050$ and, as in the static case, averaged over 50 configurations.

In Fig. 4, we show the effect of disorder and interactions on the time-dependent density, when $b_S(t)$ has been applied, with $b_0 = 1.5$. The chemical potential in the system was chosen to have half filling in the leads (i.e., $n = n_\uparrow + n_\downarrow = 1$). For convenience, we show the deviation of the density $\Delta n_i = n_i(\tau) - n_i(0)$, rather than the density itself, since it illustrates more directly the changes in the system. The left panel of Fig. 4 corresponds to when neither disorder nor interactions are present in the chain. In the transient phase, for sites close to the biased lead, we observe a quite sharp rise of the density, while the change in density occurs more smoothly for sites closer to the unbiased lead. It is also clear that the densities in the chain attain a steady-state value rather soon, already at $\tau \lesssim 15$, and that there is a quite regular propagation of the density front across the chain. Disorder modifies in a quite substantially way the situation just described. In Fig. 4(b), we note an increased Δn for sites close to the biased lead, but the profile of the density propagation front is now more irregular and significantly attenuated inside the chain. This is also observed for weaker disorder ($W = 1$, not shown), although the differences from the homogeneous case are smaller.

An interesting fact occurs when introducing interactions ($U = 4$) in the chain [Fig. 4(c)]. Now the time-dependent density landscape recovers much of the regularity of the $U = W = 0$ case, and the propagation of the density wave is considerably less attenuated [with respect to Fig. 4(a), the

values of Δn in the long-time limit are reduced]. So, it appears that even in the time-dependent case, interactions can reduce the effect of disorder. We already noted such competition of effects when discussing the IPR in the ground state, but the results of Fig. 4, and other cases we have analyzed, not shown here, confirm the robustness of this behavior with respect to (i) bias strength (we also considered $b_0 = 0.5$), (ii) particle density (we also investigated the quarter filling regime), and, of course, (iii) disorder and/or interaction strength.

3. Time-dependent inverse participation ratio

Also accessible within a KS lattice-TDDFT scheme is the time-dependent IPR, which we define via a simple modification of Eq. (52): $IPR_C^{KS}(\tau) \equiv \sum_{i \in C}[n_i^{KS}]^2(\tau)/[\sum_{i \in C} n_i^{KS}(\tau)]^2$. Results for the time-dependent IPR are shown in Fig. 5 (see the figure caption for a definition of all the parameters). From Fig. 5, we observe that a larger disorder induces a larger IPR, also in the dynamical regime. This holds for all cases examined in the figure; at the same time, for a fixed disorder strength, interactions make the system more delocalized in time (as before, a complete delocalization corresponds to an IPR $= 1/L = 0.06$). At long times, the IPR is reduced compared to its initial value; such decrease is almost monotonic for large W, while at smaller disorder strengths the IPR grows at first and then eventually becomes smaller. The region of increased IPR corresponds to the transient phase, where the variance among the different densities in the chain is largest (we have verified that the position at which the IPR attains its maximum value depends on the way the bias is ramped up). Conversely, the small IPR at long times shows that, on average, the densities have the least mutual variance in a regime where a steady-state current can be attained.

4. Time-dependent currents and the steady-state regime

A more direct way to look at the competition of disorder and interactions in the dynamical regime is analyzing the behavior of the current (in our case, the charge current). In Fig. 6, we present results for the average current at the leftmost-bond in the chain. Altogether, the different panels of Fig. 6 show
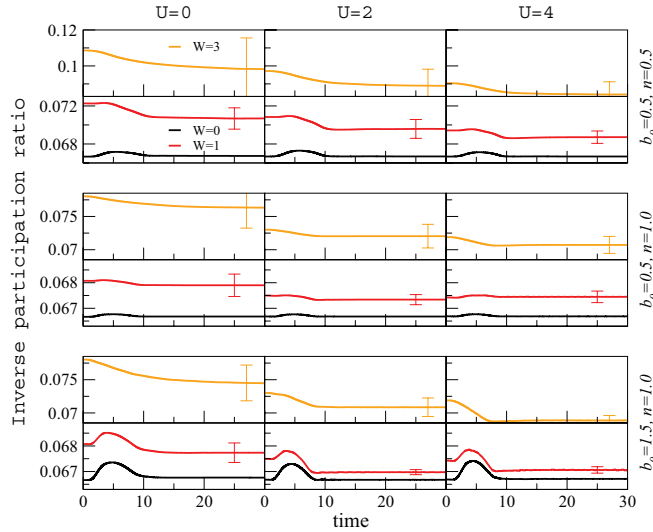
FIG. 5. (Color online) Time-dependent IPR for a disordered and interacting chain with $L = 15$ sites, contacted to semi-infinite leads. Results are shown for different values of box disorder (W), interaction (U), bias (b_0) strengths and for different lead densities n. Arithmetical disorder averaging is performed over 50 configurations. Panels with one (orange) curve refer to the case of $W = 3$, while those with two (black and red) curves refer to $W = 0$ and $W = 1$, respectively. Panels in the same column pertain to the same interaction value U, while panels in a row refer to common values of b_0 and n, as specified on the right of that row. All panels share the same horizontal time interval, but scales on the vertical axes are different. For $W > 0$, the inherent standard deviations in the long-time limit are shown as vertical bars.

the current for several values of disorder/interaction strengths, of the biases, and the band filling (see the figure caption for details on how the results are presented). We start with panel (a), corresponding to $U = 0$, a bias $b_0 = 0.5$, and a density (in the leads) $n = 0.5$ (quarter filling). For $W = 0$ (black curve), the current reaches its steady-state value after a relatively short transient. On adding disorder ($W = 1$, red curve), the length of transient increases, but eventually a steady state is reached. On further increasing W, a steady-state current is not reached within the simulation window (orange curve). However, the current in Fig. 6 (orange curve) and the currents at the other bonds in the chain (not shown) become progressively close to the same average value (with smooth and decaying oscillations), suggesting that a steady state is reached outside our simulation window. The overall trend in panel (a) is that an increasing disorder reduces the long-time (steady-state) value of the current. Analogous behavior is seen in panels (a) and (b) of the $U = 0$ column, which correspond to different choices of the bias b_0 and the density n in the leads. Moving to the other two columns ($U = 2, 4$), we see that the changes in each panel follow the same pattern, namely when disorder increases the current gets reduced.

A different perspective emerges from Fig. 6 when we mutually compare panels within the same row [e.g., panels (a), (d), and (g)]. In this case, for a given value of disorder strength, bias, and density, the current increases at larger values of U, an effect of competing disorder and interaction in the nonequilibrium regime. In the first row of Fig. 6 the current is always increasing when U becomes larger, independently of
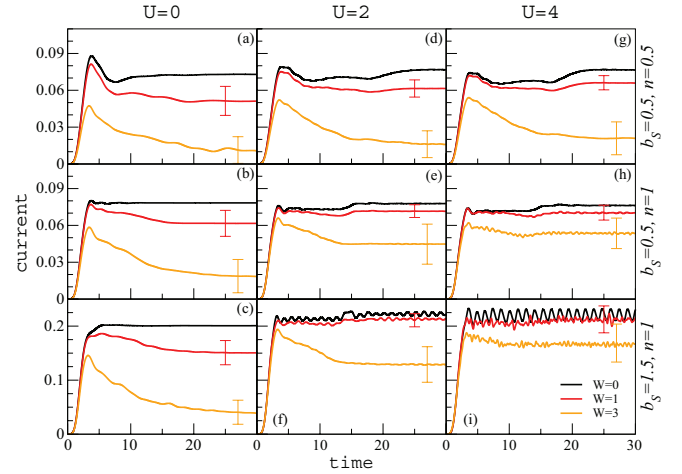

FIG. 6. (Color online) Time-dependent average currents for a chain with $L = 15$ sites, and different interactions strengths ($U = 0, 2, 4$). The currents shown are computed at the leftmost bond in the chain. On the horizontal axis, the time is expressed in units of the inverse hopping parameter. The bias and the band filling for panels in the same row are specified on the right, while in each panel, the current is displayed for three disorder strengths ($W = 0, 1, 3$). Color coding for all panels is specified in the right lowermost panel. The configuration averages were obtained from 50 instances of box disorder. For $W > 0$, the inherent standard deviations in the long-time limit are shown as vertical bars.

the value of W. Conversely, in the other two rows, depending on the value of W, the current can have a nonmonotonic dependence on U. Such nonmonotonic (dynamical) behavior is consistent with results from ground-state studies (see, e.g., Ref. 116), and its dependence on quantities such as the density n or the disorder strength W is plausible. To have a more complete picture of this tendency, calculations for larger U values should be performed; however, as mentioned earlier, for those U values, the utility of an ALDA-TDDFT approach would be significantly diminished.

So far, we have not mentioned at all the oscillatory behavior of the current in some of the panels of Fig. 6. Current and/or density oscillations in the long-time limit can result from different factors, such as single-particle bound states[122,123] (in our case, due to diagonal disorder), discontinuities in the XC potential,[74] or a sloshing motion of the charge between different regions of the device and/or the terminal sites of the leads. This latter mechanism has been pointed out and analyzed in a study[127] of the dynamical effects of image charge in quantum transport. In our system, we have observed that different and independent sets of oscillations can emerge in different parts of the chain, due to the inhomogeneities in the energetic landscape introduced by disorder (current and cumulative density oscillations are more/less pronounced in different subregions of the chain). In recent work,[71,111,127] Hartree-Fock and TDDFT-ALDA approaches have been compared to results from Kadanoff-Baym dynamics. These studies clearly point out the importance of nonlocal (in space and time) contribution beyond the instantaneous density and suggest[111,112,127] that current/density oscillations of the kind mentioned above are likely fragile against the inclusion of memory effects. We wish to add here that, for disordered systems, another obvious cause

of dephasing of the oscillations is disorder averaging. This can be argued already at the noninteracting level. While bound states can certainly be present in a specific instance of disorder, the induced oscillations are most probably to be washed out by configuration averaging, due to destructive interference among the oscillation from different configurations. This receives indirect support from observing that already in the ground state of a device with binary disorder (Fig. 3), split-off structures are largely reduced or washed out by exact or CPA averaging. In our time-dependent calculations, as commonly done in the literature, configuration averages are based on a limited (and thus incomplete) number of random disorder realization; in this case the aforementioned cancellation effects of the oscillations can be incomplete. In any case, the feature emerging from our calculations, namely a competition between disorder and interaction, appears to unrelated to current oscillations, since it present itself also when such oscillations are missing [see, e.g., in panels (a), (d), and (g) in Fig. 6].

As a final, but important remark, we observe that our results for the current lack of "reciprocity," i.e., for a fixed U and the Ws considered, the current is monotonically decreasing as a function of W, while a competing behavior could be expected from studies in the ground state.[116] This can possibly be due to a limitation of the ALDA (and not of TDDFT, which is, in principle, an exact theory). At the same time, we wish to point out that, out of equilibrium and in the nonlinear regime, the strength of the bias b_0 can also significantly influence the competition between disorder and interactions [results for $b_0 = 1.5, n = 0.5$, not shown here, compared to those in panels (a), (d), and (g), are consistent with this assertion].

D. Arithmetic averages and large fluctuations

In the other sections of this paper, the effect of disorder is discussed in terms of arithmetic averages over an incomplete/complete set of disorder configurations. This is certainly plausible when the system under investigation exhibits self-averaging behavior over disorder, i.e., when the fluctuations around its "average" behavior become negligible. The contacted, disordered wires considered in this work are quite small and thus are not expected to exhibit self-averaging behavior. For longer wires, one can expect that the deviations will decrease; such systematic studies are, however, beyond our present scope. Thus, for the wires studied here, if the fluctuations are large, the use of arithmetic averages could be questionable.

The standard deviation of IPRs and currents in the long-time limit was shown in Figs. 5 and 6. The results, which are well converged with respect to the number of configurations, indicate that the sample-to-sample fluctuations in the current are far from negligible and in some cases even comparable to the average current itself (for the IPR, the relative fluctuations are considerably smaller, see below). Even if the disorder-induced current increase is larger than the standard deviations in some cases, one could argue that the large fluctuations could cast doubts on our conclusions from Sec. VI C, concerning the competition between disorder and interactions. However, as we show next, the trends in our results are robust against the lack of self-averaging and so are the general conclusions of our work.

In the absence of self-averaging, the appropriate way to characterize an observable f in the presence of disorder is to consider the full probability distribution $P(f)$ of its outcomes.[4] If it is only possible to use a single representative value, one can then consider the value f_{typ}, corresponding to the maximum of $P(f)$: This is the "typical" value of f, with the highest probability of occurrence. These arguments play a central role in describing disorder-induced metal-insulator transitions (see, e.g., Refs. 116,128,129) where the key quantity (also in the presence of interactions), i.e., the order parameter, is the typical LDOS, which vanishes at the transition.[128] The LDOS distribution approximately agrees with a log-normal distribution,[81] with values spread over a wide range and with a long tail of low-probability outcomes (hence, the standard deviation from the arithmetically averaged LDOS is large). The geometrical average $\langle f \rangle_g = e^{\langle \ln f \rangle_a}$ (where $\langle \cdots \rangle_a$ denotes the arithmetic average) is the median of a log-normal distribution and is used as a reasonable, approximate estimate to the typical LDOS[81,116,128,129]: In particular, if the typical value of (approximately log-normal) LDOS distribution reduces to zero (when disorder increases), the geometric average also vanishes at a critical disorder strength, thus being able to monitor/characterize the metal-insulator transition.

We now further investigate our system(s) while taking into account the lack of self-averaging and employing the statistical notions just introduced. Furthermore, we explicitly focus on a subset of the cases discussed earlier (those not shown give similar results and indications). The disorder configurations we use are the 50 ones already considered for arithmetical averaging.

Figures 7(a)–7(c) illustrate the frequency distribution of the steady-state currents for half filling with a bias $b_S = 0.5$, as a function of the interaction- and disorder-strength [as in Figs. 6(b), 6(e), and 6(h)]. The current distributions (histograms are used for visual convenience, but simple scatter
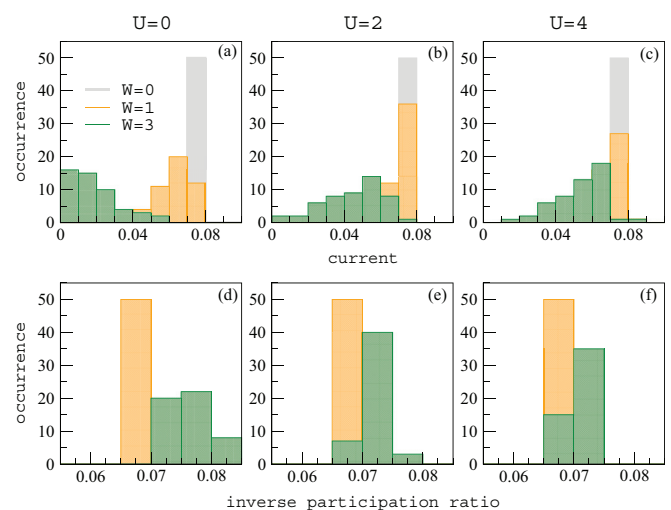

FIG. 7. (Color online) Probability distribution of currents and IPRs in the long-time limit for half-filled leads with bias $b_S = 0.5$. The legend in panel (a) applies to all panels. In (d)–(f), the $W = 0$ bars are beneath the $W = 1$ ones. The absolute spread in IPR for $W = 1$ is much smaller than for $W = 3$. Thus, on the scale of the figure, the IPR for $W = 1$ fall into a single bin.

plots exhibit the same behavior) clearly indicate a progressive increase of the "typical" current when interactions are added in the presence of disorder.

The same occurs for the IPR, Figs. 7(d)–7(f): For larger interactions, the IPR becomes smaller, indicative of a lesser degree of localization. We also note that the spread of the IPR values tends to be less than for the currents, which could be because the IPR is an integrated (over the density) quantity. When the fluctuation becomes small, geometrical and arithmetic averages assume similar values [as already noted in relation to Fig. 1(g)], since, for small σ, $\langle f \rangle_g \simeq \langle f \rangle_a e^{-\frac{1}{2}[\sigma/\langle f \rangle_a]^2}$.

The interplay between interactions and disorder in our contacted chains could also be characterized by other quantities, such as transmission functions, conductances, and LDOSs. For transmission functions and conductances, we plan to present a detailed analysis elsewhere (the relation between many-body and KS conductances was briefly discussed in Sec. VI A); here we just mention that preliminary results for these two quantities also suggest the same kind of interplay between disorder and interactions. On the other hand, for the LDOS, the effect of disorder was already considered in connection with our discussion of the CPA, Sec. VI B. Here, for completeness, we add the case of the geometric averages. To this end, we refer back to the inset panel of Fig. 3, where the geometrically averaged LDOS is shown. It clearly seen that for $U = 0$ the LDOS is reduced by disorder but, if present, interactions can revert the trend (this applies to all the sites in the chain).

To summarize, in this section we have examined the effects of disorder while taking into account the lack of self-averaging in our system(s). The discussion was confined to selected cases and quantities, which, however, are representative of the situation in general (and of the other results not shown). The analysis of the current and IPR distribution functions, and the use of geometrical averages, gave evidence consistent with that obtained via arithmetic averages, namely that interactions can dynamically reduce localization induced by disorder.

E. Isolated short chains: TDDFT and exact results

The quantum transport results just discussed are based on approximate XC potentials, obtained via an (adiabatic) LDA to v_{xc}. Comparisons between exact and (A)LDA results have been performed before in different contexts,[32,41,62,71,111] but without considering the case of interest here, namely configuration-averaged quantities in disordered and interacting samples contacted to semi-infinite leads.

An ideal way of doing this would be to use time-dependent DMRG results as benchmark to obtain a comprehensive assessment of lattice (TD)DFT for the transient behavior of current and densities. From the computational point of view, these kinds of investigations are expected to be rather expensive, and we are not aware of any published work on the subject. Here we take a much simpler view and consider small isolated disordered and isolated chains with few electrons, which can be treated via exact diagonalization. An extensive comparison between exact and lattice (TD)DFT results is outside the scope of this work, and we briefly discuss just one example, using a single case to gain some general insight.
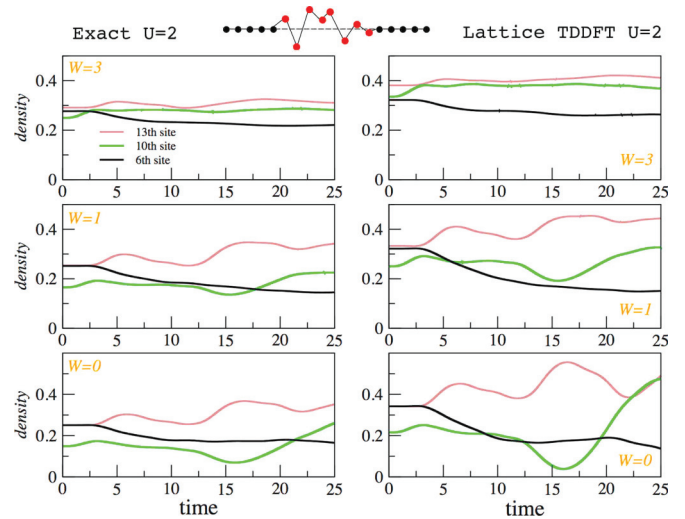

FIG. 8. (Color online) Exact (left panels) vs lattice TDDFT (right panels) averaged density results for an isolated chain with $L = 18$ sites and $U = 2$. The chain has a central region of eight sites, with disorder and interaction, and two finite "leads" of five sites each (see the schematic rendering). In the chain there are $N = 4$, spin-compensated particles and the dynamics is induced with a time-dependent "bias" which is uniformly applied to the nine leftmost sites. The time dependence of the bias is the same as that of Eq. (53), with strength $b_0 = 0.5$. The color coding in the top left panel applies to all panels in the figure. The disorder averaged densities were obtained using 100 disorder configurations.

In Fig. 8, we examine the time-dependent densities, for a short isolated cluster (all the parameters are specified in the figure caption). We mention that, differently from the previous sections, the "bias" is applied on the left half of the cluster, i.e., also in part of the interacting, disordered region (see the schematic rendering in at the top of Fig. 8). Also, due to the small size of our system, several reflections at the cluster boundary occur during the simulation interval considered in Fig. 8. Without going into any detail, the salient features emerging from Fig. 8 are that TDDFT performs better at larger disorder strength, and that, compared to the exact results, TDDFT enhances the spread among the time-evolved densities. From this example, it is apparent that lattice (TD)DFT is able to reproduce the qualitative behavior of the exact results, but good quantitative agreement is lacking. More investigations in this direction and an improvement of the XC potentials are certainly required.

VII. CONCLUSIONS

We have used lattice TDDFT to study the quantum transport properties of short, disordered, and interacting chains contacted to semi-infinite leads. Our work is largely exploratory in character, since we have addressed only superficially several issues connected to the nonequilibrium physics of disordered interacting systems.

In principle, TDDFT is an exact approach, but (at times severe) approximations are usually made for the key quantity of the approach, the XC potential. We have employed one of them, the ALDA. Disordered systems, with a strongly

varying local environment, are quite difficult tests for the ALDA which, however, by comparison to exact benchmarks, certainly appears appropriate at the qualitative level for not too-fast varying time-dependent perturbations.

Within these boundaries, we have been able to address a type of system which is not easily accessible, for one reason or another (limitations in principle, numerical costs, dimensionality, etc.) to several of the other methods currently available. In fact, we are not aware of any existing work for the quantum transport geometries considered here, where, in the presence of semi-infinite contacts, currents and densities in the disordered and correlated sample have been followed in time from the initial transient phase to the long-time (possibly steady-state) regime. To perform our study, we have introduced some modifications to the formalism and modified the definition of one of the standard indicators of localization, the IPR. We have also explored the performance of the CPA, one of the popular schemes for performing disorder averaging. The sharp spectral features due to disorder in the device are exceedingly smoothed by the CPA, and this can affect the behavior of the averaged steady-state currents.

Our time-dependent results show rather evident signatures of dynamical delocalization due to the dynamical competition of disorder and interaction in the sample. This is consistent with the qualitative picture usually adopted for systems in the ground state, where interactions produce a "screening" of the disorder; i.e., the "attractive" behavior of low-energy impurities is compensated by the local repulsive interactions, thus providing a less corrugated energy landscape. However, in the present case, an additional role is played by the (nonweak) electric bias in the lead(s), which significantly (and dynamically) modifies the ground-state energy landscape and wave functions.

To what extent our findings remain robust against an improvement of the XC potentials is at present an open question. For example, a recent investigation[112] has shown the importance of long-ranged nonequilibrium XC potentials, extending far away in the leads, which arise after the bias is applied. This can cast reservations on quantitative results based on the ALDA. However, with approximate XC potentials, it should still be possible to address qualitative issues, as done here, where one is studying the general trends of the competition between disorder and interactions. More in general, the current state of affairs certainly calls for better potentials and future investigations, hopefully combined also with other methods. In this respect, we are currently carrying out a study of disorder and correlation effects in quantum transport using the time-dependent KBEs (where interactions are treated within many-body approximate schemes, but non-local, nonadiabatic effects are taken into account). Preliminary results for very short chains confirm the trends observed in this work with lattice (TD)DFT.

APPENDIX A: LANCZOS TIME PROPAGATION

We briefly summarize the Lanczos method, as given in Ref. 114. A useful comparative study between the Lanczos method and other integration schemes can be found in Ref. 130. Consider a system described by a TD Hamiltonian $H(t)$. If, for example, we use the midpoint approximation for the time propagator and wish to evolve the system in the time interval $(t + \Delta, t)$, we obtain

$$|\Phi_{t+\Delta}\rangle = e^{-iH(t+\Delta/2)\Delta}|\Phi_t\rangle, \tag{A1}$$

where $|\Phi_t\rangle$ is the (known) initial wave function. Consider a finite Lanczos sequence $\{|V_k\rangle\}$, obtained by starting acting on the "seed" $|\Phi_t\rangle \equiv |V_0\rangle$. Using $\{|V_k\rangle\}$ as a truncated basis, we get

$$|\Phi_{t+\Delta}\rangle \approx \sum_{k=0}^{M_L} |V_k\rangle \langle V_k|e^{-iH_L t}|V_0\rangle, \tag{A2}$$

where H_L is the tridiagonal representation for $H(t + \Delta/2)$ in such a basis. Inserting a complete set of eigenstates for the truncated space, $H_L|\lambda\rangle = \epsilon_\lambda|\lambda\rangle$,

$$|\Phi_{t+\Delta}\rangle = \sum_{k=0}^{K} |V_k\rangle \left[\sum_\lambda \langle V_k|\lambda\rangle e^{-i\epsilon_\lambda t}\langle\lambda|V_0\rangle \right], \tag{A3}$$

where $|\Psi_{t+\Delta}\rangle$ is finally expressed in the basis of the original many-body Hamiltonian. The method requires a partial orthogonalization on the fly of the Lanczos basis in order to preserve accuracy along the trajectory. For a simple estimate of the truncation error in Eq. (A2), see the discussion in Ref. 114.

APPENDIX B: COMPUTATIONALLY EFFICIENT LORENTZIAN SUMS

To determine the energy-dependent IPR of a finite system using the N_λ eigenstates/values of the Hamiltonian, we have to determine the LDOS $n(\omega) = \sum_\lambda c^\lambda \delta(\omega - \epsilon_\lambda)$. This has to be done for the N_ω values of the chosen energy grid. Furthermore, in some cases (as in our work here) the IPR is also averaged over N_D disorder configurations. Since the system is finite, it is expedient to introduce a Lorentzian broadening Γ, and to define a broadened LDOS,

$$n^\Gamma(\omega) \equiv n(\omega) * L^\Gamma(\omega) = \sum_\lambda c^\lambda L^\Gamma(\omega - \epsilon_\lambda), \tag{B1}$$

where $L^\Gamma(\omega) = (\Gamma/\pi)(\omega^2 + \Gamma^2)^{-1}$. When N_λ, N_ω, N_D are large, to compute $n^\Gamma(\omega)$ directly from Eq. (B1) can be computationally intensive. Fast Fourier transform (FFT) is the method of choice in these cases, but it requires uniform sampling, while the eigenvalues poles ϵ_λ are in general unevenly distributed. This issue can be avoided with the approach described here, which is fast and accurate, and, in principle, should be relevant to FFT integration problems for a large data set from nonuniform, adaptive, or curvilinear sampling.[131] To begin with, it is convenient to have a smooth function $C^\gamma(\omega)$ that decays rapidly in both ω and t spaces, minimizes ω sampling, and allows smooth uniform sampling of $n^{C^\gamma}(\omega) = n(\omega) * C^\gamma(\omega)$. Then, the actual procedure is as follows: (i) we sample $n^{C^\gamma}(\omega), L^\Gamma(\omega), C^\gamma(\omega)$; (ii) via FFT, we compute $n^{C^\gamma}(t), L^\Gamma(t), C^\gamma(t)$; (iii) we obtain

$n^\Gamma(t) = [n^{C^\gamma}(t)/C^\gamma(t)] \times L^\Gamma(t)$; (iv) via inverse FFT, we compute $n^\Gamma(\omega)$.

The softening function C^γ should be positive definite in both ω, t spaces to ensure easy deconvolution (we discard band-limited functions such as rectangle, triangle, etc., since they require careful location of their zeros). We also discard $C^{\tilde\gamma} = \exp(-\gamma\omega^2)$, since (a) $C^\gamma(t)$ may decay too fast, with deconvolution instabilities where $L^\Gamma(t)$ is still non-negligible; (b) it is still expensive to determine $n(\omega) * \exp(-\gamma\omega^2)$ on N_ω sampling points. Based on these considerations, our optimal choice is

$$\tilde{C}^\gamma(\omega) = \frac{\gamma}{4}\left(1 - \gamma\frac{\partial}{\partial\gamma}\right)e^{-\gamma|\omega|} \propto e^{-\gamma|\omega|} * e^{-\gamma|\omega|}. \quad \text{(B2)}$$

The function $\tilde{C}^\gamma(\omega)$ decays exponentially, i.e., is "practically" band limited with a small sampling domain; $\tilde{C}^\gamma(t) \propto (t^2 +$

$\gamma^2)^{-2}$ is always positive, and it decays slower than $L^\Gamma(t)$, thus avoiding deconvolution instabilities. Also, as results from the self-convolution in the definition of C^γ, the cusp $e^{-\gamma|\omega-\epsilon_\lambda|}$, when ϵ_λ is off grid, is smoothed, reducing sampling errors. Finally, as a crucial advantage of the method, $n^{C^\gamma}(\omega)$ can be computed recursively, needing the λ sum just once (instead of at all the sampling points). In fact, writing $n^{\tilde{C}^\gamma}(\omega) = \tilde{n}_+(\omega) + \tilde{n}_-(\omega)$, with $n_\pm(\omega) = \sum_\lambda c^\lambda e^{\pm\gamma(\omega-\epsilon_\lambda)}\Theta(\pm(\epsilon_\lambda - \omega))$, we get ($\Theta$ is the Heaviside function)

$$\tilde{n}_\pm(\omega \mp \Delta) = e^{-\gamma\Delta}[\tilde{n}_\pm(\omega) + \gamma\Delta n_\pm(\omega)]$$
$$+ \left(1 - \gamma\frac{\partial}{\partial\gamma}\right) \times \sum_\lambda c^\lambda e^{\pm\gamma(\omega-\epsilon_\lambda\mp\Delta)}$$
$$\times \Theta(\pm(\omega - \epsilon_\lambda))\Theta(\Delta \pm (\epsilon_\lambda - \omega)). \quad \text{(B3)}$$

---

[1] S. Datta, *Electronic Transport in Mesoscopic Systems* (Cambridge University Press, Cambridge, UK, 1995).

[2] J. R. Heath and M. A. Ratner, Phys. Today **56**, 43 (2003).

[3] M. Di Ventra, *Electrical Transport in Nanoscale Systems* (Cambridge University Press, Cambridge, UK, 2008).

[4] P. W. Anderson, Phys. Rev. **109**, 1492 (1958).

[5] N. F. Mott and W. D. Twose, Adv. Phys. **10**, 107 (1961).

[6] P. Lloyd, J. Phys. C: Solid State Phys. **2**, 1717 (1969).

[7] J. T. Edwards and D. J. Thouless, J. Phys. C: Solid State Phys. **5**, 807 (1972).

[8] J. M. Ziman, *Models of Disorder* (Cambridge University Press, Cambridge, UK, 1979).

[9] E. Abrahams, P. W. Anderson, D. C. Licciardello, and T. V. Ramakrishnan, Phys. Rev. Lett. **42**, 673 (1979).

[10] M. Ma, Phys. Rev. B **26**, 5097 (1982).

[11] B. Kramer and A. MacKinnon, Rep. Prog. Phys. **56**, 1469 (1993).

[12] J. B. Pendry, Adv. Phys. **43**, 461 (1994).

[13] U. Gavish and Y. Castin, Phys. Rev. Lett. **95**, 020401 (2005).

[14] R. T. Scalettar, AIP Conf. Proc. **918**, 111 (2007).

[15] F. Evers and A. D. Mirlin, Rev. Mod. Phys. **80**, 1355 (2008).

[16] K. Byczuk, W. Hofstetter, and D. Vollhardt, Int. J. Mod. Phys. B **24**, 1727 (2010).

[17] See, e.g., W. S. Dias, E. M. Nascimento, M. L. Lyra, and F. A. B. F. de Moura, Phys. Rev. B **81**, 045116 (2010).

[18] For recent experimental work, see B. Deissler, M. Zaccanti, G. Roati, C. D'Errico, M. Fattori, M. Modugno, G. Modugno, and M. Inguscio, Nat. Phys. **6**, 354 (2010).

[19] C. W. J. Beenakker, Rev. Mod. Phys. **69**, 731 (1997).

[20] P. Hohenberg and W. Kohn, Phys. Rev. **136**, B864 (1964); W. Kohn and L. J. Sham, *ibid.* **140**, A1133 (1965).

[21] E. Runge and E. K. U. Gross, Phys. Rev. Lett. **52**, 997 (1984).

[22] For alternative proofs of the basic theorems of TDDFT[21] for continuum systems, see, e.g., R. van Leeuwen, Phys. Rev. Lett. **82**, 3863 (1999); M. Ruggenthaler and R. van Leeuwen, Europhys. Lett. **95**, 13001 (2011); M. Ruggenthaler, K. J. H. Giesbertz, M. Penz, and R. van Leeuwen, Phys. Rev. A **85**, 052504 (2012).

[23] M. A. L. Marques, C. A. Ullrich, F. Nogueira, A. Rubio, K. Burke, and E. K. U. Gross (eds.), *Time-Dependent Density-Functional Theory* (Springer Verlag, Berlin, 2006).

[24] M. A. L. Marques, N. T. Maitra, F. M. S. Nogueira, E. K. U. Gross, and A. Rubio (eds.), *Fundamentals of Time-Dependent Density-Functional Theory* (Springer Verlag, Berlin, 2012).

[25] C. A. Ullrich, *Time-Dependent Density-Functional Theory: Concepts and Applications* (Oxford University Press, Oxford, UK, 2012).

[26] O. Gunnarsson and K. Schönhammer, Phys. Rev. Lett. **56**, 1968 (1986).

[27] K. Schönhammer and O. Gunnarsson, J. Phys. C: Solid State Phys. **20**, 3675 (1987).

[28] K. Schönhammer and O. Gunnarsson, Phys. Rev. B **37**, 3128 (1988).

[29] K. Schönhammer, O. Gunnarsson, and R. M. Noack, Phys. Rev. B **52**, 2504 (1995).

[30] N. A. Lima, M. F. Silva, L. N. Oliveira, and K. Capelle, Phys. Rev. Lett. **90**, 146402 (2003).

[31] N. A. Lima, L. N. Oliveira, and K. Capelle, Europhys. Lett. **60**, 601 (2002).

[32] G. Xianlong, M. Polini, M. P. Tosi, V. L. Campo, K. Capelle, and M. Rigol, Phys. Rev. B **73**, 165120 (2006).

[33] X. L. Gao, M. Polini, M. P. Tosi, and B. Tanatar, Int. J. Mod. Phys. B **22**, 4500 (2008).

[34] V. L. Campo, Jr. and K. Capelle, Phys. Rev. A **72**, 061602(R) (2005).

[35] E. Perfetto and G. Stefanucci, Phys. Rev. B **86**, 081409(R) (2012).

[36] J. Lorenzana, Z.-J. Ying, and V. Brosco, Phys. Rev. B **86**, 075131 (2012).

[37] V. V. França, D. Vieira, and K. Capelle, New J. Phys. **14**, 073021 (2012).

[38] V. L. Campo, K. Capelle, C. Hooley, J. Quintanilla, and V. W. Scarola, Phys. Rev. A **85**, 033644 (2012).

[39] X. Gao, A. Hai Chen, I. V. Tokatly, and S. Kurth, Phys. Rev. B **86**, 235139 (2012).

[40] R. Baer, J. Chem. Phys. **128**, 044103 (2008).

[41] C. Verdozzi, Phys. Rev. Lett. **101**, 166401 (2008).

[42] Y. Li and C. A. Ullrich, J. Chem. Phys. **129**, 044105 (2008).

[43] W. Li, G. Xianlong, C. Kollath, and M. Polini, Phys. Rev. B **78**, 195109 (2008).

[44] S. Kurth and G. Stefanucci, Chem. Phys. **391**, 164 (2011).

[45] G. Stefanucci, E. Perfetto, and M. Cini, Phys. Rev. B **81**, 115446 (2010).

[46]I. V. Tokatly, Phys. Rev. B **83**, 035127 (2011).

[47]M. Farzanehpour and I. V. Tokatly, Phys. Rev. B **86**, 125130 (2012).

[48]S. Kurth, G. Stefanucci, C.-O. Almbladh, A. Rubio, and E. K. U. Gross, Phys. Rev. B **72**, 035308 (2005).

[49]J. Hubbard, Proc. R. Soc. A **276**, 238 (1963).

[50]M. F. Silva, N. A. Lima, A. L. Malvezzi, and K. Capelle, Phys. Rev. B **71**, 125130 (2005).

[51]V. V. França and K. Capelle, Phys. Rev. A **74**, 042325 (2006); Phys. Rev. Lett. **100**, 070403 (2008).

[52]A. Schindlmayr and R. W. Godby, Phys. Rev. B **51**, 10427 (1995).

[53]M. Saubanère and G. M. Pastor, Phys. Rev. B **79**, 235101 (2009).

[54]R. Requist and O. Pankratov, Phys. Rev. A **81**, 042519 (2010).

[55]A. Akande and S. Sanvito, Phys. Rev. B **82**, 245114 (2010).

[56]V. Brosco, Z. Ying, and J. Lorenzana, arXiv:1208.4322.

[57]D. J. Carrascal and J. Ferrer, Phys. Rev. B **85**, 045110 (2012).

[58]G. Stefanucci and S. Kurth, Phys. Rev. Lett. **107**, 216401 (2011).

[59]J. H. Hu, J.-J. Wang, G. Xianlong, M. Okumura, R. Igarashi, S. Yamada, and M. Machida, Phys. Rev. B **82**, 014202 (2010).

[60]X. Gao, Phys. Rev. B **81**, 104306 (2010).

[61]D. Karlsson, C. Verdozzi, M. M. Odashima, and K. Capelle, Europhys. Lett. **93**, 23003 (2011).

[62]D. Karlsson, A. Privitera, and C. Verdozzi, Phys. Rev. Lett. **106**, 116401 (2011).

[63]D. Jaksch and P. Zoller, Ann. Phys. **315**, 52 (2005).

[64]M. Ijäs and A. Harju, Phys. Rev. B **82**, 235111 (2010).

[65]W. Metzner and D. Vollhardt, Phys. Rev. Lett. **62**, 324 (1989).

[66]A. Georges, G. Kotliar, W. Krauth, and M. Rozenberg, Rev. Mod. Phys. **68**, 13 (1996).

[67]F. Aryasetiawan, O. Gunnarsson, and A. Rubio, Europhys. Lett. **57**, 683 (2002).

[68]F. Aryasetiawan and O. Gunnarsson, Phys. Rev. B **66**, 165119 (2002).

[69]R. J. Magyar, Phys. Rev. B **79**, 195127 (2009).

[70]A. Zangwill and P. Soven, Phys. Rev. A **21**, 1561 (1980).

[71]C. Verdozzi, D. Karlsson, M. Puig von Friesen, C.-O. Almbladh, and U. von Barth, Chem. Phys. **391**, 37 (2011).

[72]The two treatments are, of course, equivalent when no approximations are introduced.

[73]E. H. Lieb and F. Y. Wu, Phys. Rev. Lett. **20**, 1445 (1968).

[74]S. Kurth, G. Stefanucci, E. Khosravi, C. Verdozzi, and E. K. U. Gross, Phys. Rev. Lett. **104**, 236801 (2010).

[75]J. P. Bergfield, Z. F. Liu, K. Burke, and C. A. Stafford, Phys. Rev. Lett. **108**, 066801 (2012).

[76]F. Evers and P. Schmitteckert, Phys. Chem. Chem. Phys. **13**, 14417 (2011).

[77]Z. F. Liu, J. P. Bergfield, K. Burke, and C. A. Stafford, Phys. Rev. B **85**, 155117 (2012).

[78]F. J. Wegner, Z. Phys. B **36**, 209 (1980).

[79]B. Srinivasan, G. Benenti, and D. L. Shepelyansky, Phys. Rev. B **67**, 205112 (2003).

[80]Y. Song, R. Wortis, and W. A. Atkinson, Phys. Rev. B **77**, 054202 (2008).

[81]G. Schubert, J. Schleede, K. Byczuk, H. Fehske, and D. Vollhardt, Phys. Rev. B **81**, 155106 (2010).

[82]N. C. Murphy, R. Wortis, and W. A. Atkinson, Phys. Rev. B **83**, 184206 (2011).

[83]S. Johri and R. N. Bhatt, Phys. Rev. Lett. **109**, 076402 (2012).

[84]J. Hubbard, Proc. R. Soc. Lond. A **281**, 401 (1964).

[85]P. Soven, Phys. Rev. **156**, 809 (1967).

[86]R. J. Elliott, J. A. Krumhansl, and P. Leath, Rev. Mod. Phys. **45**, 465 (1974).

[87]H. Matsuda, in *The Structure and Properties of Matter*, Springer Series in Solid State Sciences Vol. 28 (Springer, Berlin, 1982).

[88]G. Rickayzen, *Green's Functions and Condensed Matter* (Academic Press, San Diego, 1984).

[89]V. Janis and D. Vollhardt, Phys. Rev. B **46**, 15712 (1992).

[90]R. Alben, M. Blume, and M. McKeown, Phys. Rev. B **16**, 3829 (1977).

[91]V. Drchal, J. Phys. Chem. Solids **40**, 393 (1979).

[92]C. Verdozzi, P. J. Durham, R. J. Cole, and P. Weightman, Phys. Rev. B **55**, 16143 (1997).

[93]In our case, $\sigma_L = \sigma_R$, with $2\sigma_R(x) = x - \mathrm{sgn}(x)\sqrt{x^2 - 4}$ when $|x| > 2$, and $2\sigma_R(x) = x - i\sqrt{4 - x^2}$ for $x \leqslant 2$.

[94]M. Ye. Zhuravlev, A. V. Vedyayev, K. D. Belashchenko, and E. Y. Tsymbal, Phys. Rev. B **85**, 115134 (2012).

[95]For a recent review of CPA, see, e.g., D. A. Rowlands, Rep. Prog. Phys. **72**, 086501 (2009).

[96]For clarity, we mention that the initial KS state for our transport calculations is not obtained in terms of these equations, but with a different procedure, the one described in Ref. 48.

[97]N. Bushong, N. Sai, and M. Di Ventra, Nanoletters **5**, 2569 (2005).

[98]C. C. Chien, M. Zwolak, and M. Di Ventra, Phys. Rev. A **85**, 041601(R) (2012).

[99]C. C. Chien, D. Gruss, M. Di Ventra, and M. Zwolak, arXiv:1203.5094.

[100]M. Cini, Phys. Rev. B **22**, 5887 (1980).

[101]G. Stefanucci and C.-O. Almbladh, Phys. Rev. B **69**, 195318 (2004).

[102]P. Myöhänen, A. Stan, G. Stefanucci, and R. van Leeuwen, Europhys. Lett. **84**, 67001 (2008).

[103]G. Stefanucci and C.-O. Almbladh, Europhys. Lett. **67**, 14 (2004).

[104]C. Verdozzi, G. Stefanucci, and C.-O. Almbladh, Phys. Rev. Lett. **97**, 046603 (2006).

[105]P. Schmitteckert and F. Evers, Phys. Rev. Lett. **100**, 086401 (2008).

[106]S. Schenk, P. Schwab, M. Dzierzawa, and U. Eckern, Phys. Rev. B **83**, 115128 (2011).

[107]F. Mirjani and J. M. Thijssen, Phys. Rev. B **83**, 035415 (2011).

[108]M. Dzierzawa, U. Eckern, S. Schenk, and P. Schwab, Phys. Status Solidi B **246**, 941 (2009).

[109]A. Akande and S. Sanvito, J. Phys. Cond. Mat. **24**, 055602 (2012).

[110]A. Pertsova, M. Stamenova, and S. Sanvito, J. Phys.: Condens. Matter **25**, 105501 (2013).

[111]A.-M. Uimonen, E. Khosravi, A. Stan, G. Stefanucci, S. Kurth, R. van Leeuwen, and E. K. U. Gross, Phys. Rev. B **84**, 115103 (2011).

[112]P. Schmitteckert, M. Dzierzawa, and P. Schwab, arXiv:1205.4854 (to be published in Phys. Chem. Chem. Phys.)

[113]P. Tröster, P. Schmitteckert, and F. Evers, Phys. Rev. B **85**, 115409 (2012).

[114]T. J. Park and J. C. Light, J. Chem. Phys. **85**, 5870 (1986).

[115]An early discussion of the modified algorithm can be found in C. Verdozzi and C.-O. Almbladh, arXiv:0808.1643.

[116]J. Wernsdorfer, G. Harder, U. Schollwoeck, and W. Hofstetter, arXiv:1108.6057.

[117]H. Mera, K. Kaasbjerg, Y.-M. Niquet, and G. Stefanucci, Phys. Rev. B **81**, 035110 (2010).

[118] H. Mera and Y.-M. Niquet, Phys. Rev. Lett. **105**, 216408 (2010).

[119] P. Schmitteckert, arXiv:1302.3170.

[120] For example, disordered sample with scattering boundary conditions have been characterized in terms of transfer matrices, see, e.g., L. Molinari, J. Phys. A: Math. Gen. **30**, 983 (1997).

[121] T. Vojta, F. Epperlein, and M. Schreiber, Phys. Rev. Lett. **81**, 4212 (1998).

[122] G. Stefanucci, Phys. Rev. B **75**, 195115 (2007).

[123] E. Khosravi, S. Kurth, G. Stefanucci, and E. K. U. Gross, Appl. Phys. A **93**, 355 (2008).

[124] We have verified that the smooth character of the CPA LDOS persists for smaller (but nonzero) values of the artificial broadening.

[125] With respect to an Hartree-Fock + CPA treatment, the KS + CPA curve would result shifted to lower energies, since, irrespective of disorder, the effective interaction is reduced by the XC term.

[126] D. Vieira, H. J. P. Freire, V. L. Campo, Jr., and K. Capelle, J. Magn. Magn. Mater. **320**, E418 (2008).

[127] P. Myöhänen, R. Tuovinen, T. Korhonen, G. Stefanucci, and R. van Leeuwen, Phys. Rev. B **85**, 075105 (2012).

[128] V. Dobrosavljevic and G. Kotliar, Phys. Rev. Lett. **78**, 3943 (1997).

[129] Y. Song, W. A. Atkinson, and R. Wortis, Phys. Rev. B **76**, 045105 (2007).

[130] See A. Castro and M. A. L. Marques in Ref. 23.

[131] Preliminary aspects of this method have been considered by R. J. Cole and C. Verdozzi (unpublished).